Monthly Notices
of the
ROYAL ASTRONOMICAL SOCIETY

MNRAS **478,** 867–884 (2018) doi:10.1093/mnras/sty1101

The sdA problem – II. Photometric and spectroscopic follow-up

Ingrid Pelisoli,[1]★ S. O. Kepler,[1] D. Koester,[2] B. G. Castanheira,[3,4] A. D. Romero[1] and L. Fraga[5]

[1]*Instituto de Física, Universidade Federal do Rio Grande do Sul, 91501-900 Porto-Alegre, RS, Brazil*
[2]*Institut für Theoretische Physik und Astrophysik, Universität Kiel, D-24098 Kiel, Germany*
[3]*Baylor University, Waco, TX 76798, USA*
[4]*Department of Astronomy, University of Texas at Austin, Austin, TX 78712, USA*
[5]*Laboratório Nacional de Astrofísica LNA/MCTIC, 37504-364 Itajubá, MG, Brazil*

Accepted 2018 April 22. Received 2018 April 17; in original form 2018 February 23

ABSTRACT

The spectral classification 'subdwarf A' (sdA) is given to stars showing H-rich spectra and sub-main-sequence surface gravities, but effective temperature lower than the zero-age horizontal branch. Their evolutionary origin is an enigma. In this work, we discuss the results of follow-up observations of selected sdAs. We obtained time-resolved spectroscopy for 24 objects and time-series photometry for another 19 objects. For two targets, we report both spectroscopy and photometry observations. We confirm seven objects to be new extremely low-mass white dwarfs (ELMs), one of which is a known eclipsing star. We also find the eighth member of the pulsating ELM class.

Key words: subdwarfs – binaries: general – stars: evolution – white dwarfs.

1 INTRODUCTION

White dwarf stars are the most common outcome of single-star evolution, corresponding to the final observable evolutionary stage of all stars with initial mass below 7–10.6 $M_\odot$ (e.g. Woosley & Heger 2015), including the Sun and over 95 per cent of all stars in the Galaxy. Their relative abundance, combined with their simple structure and long cooling time-scales, makes them the perfect laboratory for modelling stellar evolution (e.g. Kalirai et al. 2008; Romero, Campos & Kepler 2015) and for population synthesis studies constraining the age and star formation history of different stellar populations (e.g. Liebert, Bergeron & Holberg 2005; Tremblay et al. 2016; Kilic et al. 2017). About 25 per cent of white dwarfs in the Galactic field are known to have a companion (Toonen et al. 2017); therefore, white dwarfs also have the potential to put constraints on binary evolution channels.

Short-period binary white dwarfs, in particular, are potential progenitors of Type Ia (Webbink 1984; Iben & Tutukov 1984) and .Ia supernovae (Bildsten et al. 2007). This fact motivated the first surveys for white dwarfs in close binaries (Robinson & Shafter 1987; Foss, Wade & Green 1991), which resulted in null detections. The first successful survey was performed by Marsh, Dhillon & Duck (1995). They noticed that the catalogue of Bergeron, Saffer & Liebert (1992) contained 14 white dwarfs with spectroscopic mass below 0.45 $M_\odot$, which cannot be formed within a Hubble time without some form of mass-loss enhancement. They were most likely the remnants of mass transfer in post-main-sequence common-envelope binaries. Indeed, Marsh et al. (1995) confirmed five out of the seven stars they probed to be in binaries. More recent studies suggest that the binary fraction of low-mass white dwarfs ($M \lesssim 0.45$ $M_\odot$) is at least 70 per cent (Brown et al. 2011a). Low-mass single systems can be explained by other mass-loss-enhancing mechanisms, such as high metallicity (D'Cruz et al. 1996) or supernova stripping (Wang & Han 2009), mass ejection caused by a massive planet (Nelemans & Tauris 1998) or merger events (Zhang & Jeffery 2012; Zhang et al. 2017). For the currently known white dwarfs with mass below 0.3 $M_\odot$, the binary fraction seems to be close to 100 per cent (Brown et al. 2016a). These systems are known as extremely-low mass white dwarfs (ELMs).

The ELM Survey (Brown et al. 2010, 2012a, 2013, 2016a; Kilic et al. 2011, 2012; Gianninas et al. 2015) made great progress in the study of these objects. 88 systems have been found, 76 of which were confirmed to be in binaries, mostly through analysis of their radial velocity (RV) variations. Seven systems were found to be pulsators, eight show ellipsoidal variations and two are eclipsing systems (Hermes et al. 2012, 2013a, 2013b; Bell et al. 2015; Kilic et al. 2015; Brown et al. 2016a). The distribution of secondary mass obtained suggests that over 95 per cent of the systems are not Type Ia supernova progenitors (Brown et al. 2016a). They are, nonetheless, strong gravitational wave sources (Kilic et al. 2012), given that most systems will merge within a Hubble time (Brown et al. 2016b). The gravitational wave radiation of the shortest orbital period systems ($P \lesssim 1$ h) may be detected directly by upcoming space-based missions such as the Laser Interferometer Space Antenna (LISA). Kilic et al. (2012) found three systems that should be detected clearly by missions like LISA in the first year of operations. Three other

★ E-mail: ingrid.pelisoli@gmail.com

systems are above the proposed 1σ detection limit after one year of observations. Even when not significantly above the detection limit, ELMs are important indicators of what the Galactic foreground may look like for these detectors. Therefore understanding the space density, period distribution and merger rate of these systems is crucial for interpreting the results of upcoming space-based gravitational wave missions and for studying the evolution of interacting binary systems.

The target selection of the ELM Survey was initially developed to find B-type hypervelocity stars (see the MMT Hypervelocity Star Survey: Brown, Geller & Kenyon 2009, 2012b, 2014), hence it favours the detection of hot ELMs ($T_{\rm eff} \gtrsim 12\,000$ K). Cooler objects ($T_{\rm eff} \lesssim 10\,000$ K) were targeted by Brown et al. (2012a). However, fewer than 5 per cent of the objects in the ELM Survey show $T_{\rm eff} \lesssim 9000$ K, while evolutionary models (Althaus, Miller Bertolami & Córsico 2013; Córsico & Althaus 2014, 2016; Istrate et al. 2016) predict that the same amount of time is spent above and below the aforementioned $T_{\rm eff}$. Although uncertainties in residual burning can influence the cooling time-scale significantly, it is still expected that 20–50 per cent of ELMs should show $T_{\rm eff} < 9000$ K (Brown, Kilic & Gianninas 2017; Pelisoli, Kepler & Koester 2017). Moreover, the ELM Survey selection criteria also favoured higher $\log g$ objects. The low $\log g$ phases happen before the object reaches the white dwarf cooling track (the objects are hence known as pre-ELMs: see e.g. Maxted et al. 2011, 2014) and are relatively quick. However, pre-ELMs are also much brighter. Assuming a spherical distribution, we found in Pelisoli et al. (2017) that there should be about a hundred detected objects with $\log g = 5$–6 for each object with $\log g = 6$–7 in a magnitude-limited survey. Hence there is clearly a missing population of cool, low-mass ELMs yet to be found, as evidenced in Fig. 1.

In an effort to retrieve these missing objects, Kepler et al. (2016) extended their white dwarf catalogue down to $\log g = 5.5$, revealing a population of objects that were dubbed subdwarf A stars (sdAs). Their spectra are dominated by hydrogen lines, suggestive of $T_{\rm eff} \sim 10\,000$ K and $4.75 < \log g < 6.5$. Brown et al. (2017) suggested that they are mainly metal-poor A/F stars in the halo with an overestimated $\log g$, given the pure hydrogen grid used to fit these objects in Kepler et al. (2016). However, as we showed in Pelisoli et al. (2018), the addition of metals to the models does not necessarily lower the estimated $\log g$. Moreover, we identified clearly the existence of two populations within the sdAs, with overlapping but distinct colour distributions, and found that at least 7 per cent of sdAs are more likely (pre-)ELMs than main-sequence stars, given their physical and kinematic parameters. The missing (pre-)ELMs are thus likely within the sdA population.

In this work, we follow up on selected sdAs to probe their binarity, with the aim of extending the population of known (pre-)ELMs to the entire space of physical parameters predicted by the evolutionary models. We obtain both time-resolved spectroscopy, to search for radial velocity (RV) variations indicating the presence of a close binary companion, and time series photometry, to look for eclipses, ellipsoidal variations or pulsations typical of ELMs. Extending the sample of known ELMs to cool temperatures and lower masses will allow us to test the evolutionary models more robustly. With a more complete sample, we will also be able to make more reliable predictions as to the contribution of the gravitational wave signals from ELMs to upcoming missions.

2 METHODS

2.1 Observations

Our observing campaign targeted bright objects with $T_{\rm eff}$ and $\log g$ in the range predicted by the evolutionary models shown in Fig. 1. Targets with high proper motion and/or high radial velocities and ELM-like colours, yielding high probability of being a (pre-)ELM according to Pelisoli et al. (2018), were prioritized. We have used the proper motions from the GPS1 catalogue (Tian et al. 2017), which contains all but one of the objects analysed here. Consistency checks were performed with the Hot Stuff for One Year (HSOY: Altmann et al. 2017) and UCAC5 (Zacharias, Finch & Frouard 2017) catalogues. We found that the proper motions agreed within the uncertainties for all objects studied here. Priority was also given to objects showing radial velocity variations in the subspectra taken by the Sloan Digital Sky Survey (SDSS). We obtained time-resolved spectroscopy for 26 targets. We have also obtained time series photometry for 21 targets in the vicinity of the instability strip by Tremblay et al. (2015) and Gianninas et al. (2015), obtained empirically taking into account 3D corrections to $T_{\rm eff}$ and $\log g$. The targets are listed in Table 1, as well as their SDSS g magnitude, proper motion (ppm), distances given a MS or (pre-)ELM radius and velocities in the Galactic rest frame ($v_{\rm los}$).

We carried out spectroscopy mainly with the Goodman Spectrograph (Clemens, Crain & Anderson 2004) on the 4.1-m Southern Astrophysical Research (SOAR) Telescope. All exposures were taken with a 1.0-arcmin slit and binned by a factor of two in both dimensions. We used a 1200 line $\rm m^{-1}$ grating, with a camera angle of 30.00° and grating angle of 16.30°, obtaining a wavelength coverage of 3600–4950 Å with a resolution of ∼2 Å.

We also obtained spectroscopy with the GMOS spectrographs (Hook et al. 2004; Gimeno et al. 2016) on both Gemini North and Gemini South 8.1-m telescopes. The exposures were taken with a 0.75-arcmin slit. As with SOAR, we binned the CCD by a factor of two in both dimensions and used a 1200 line $\rm mm^{-1}$ grating. Exposures centred at both 4400 and 4450 Å were taken for each semester, to dislocate the position of the two gaps between the CCDs in GMOS, covering wavelengths 3580–5190 and 3630–5240 Å, respectively. Our data were partially affected by the bright columns issue developed by GMOS-S CCD2 and CCD3 during 2016 September 30–2017 February 21.

Five $\log g > 5.5$ objects were observed with the medium resolution echelle spectrograph X-shooter (Vernet et al. 2011), mounted on VLT-UT2 at Paranal, Chile. X-shooter covers the spectral range from the atmospheric cut-off in the UV to the near-infrared with three separate arms: UVB (3000–5600 Å), VIS (5600–10 100 Å) and NIR (10 100–24 000 Å). The data were taken in stare mode, using slits of 1.0, 0.9 and 1.2 arcmin for UVB, VIS and NIR arms, respectively, which allows a resolution of ∼1 Å. X-shooter has the advantage of also allowing us to search for red companions, which could appear as an excess in the NIR arm spectra.

For all instruments, arc-lamp exposures were taken before and after each science exposure to verify the stability. For the wavelength calibration, a CuHeAr lamp was taken after each round of exposures, at the same position as the science frames. Due to the faintness of the objects and the need for multiple spectra, the exposure time was estimated aiming at a median signal-to-noise ratio (S/N) of 10–15 per exposure. One radial velocity standard was observed during each semester to verify the reliability of the method and a spectrophotometric standard star was

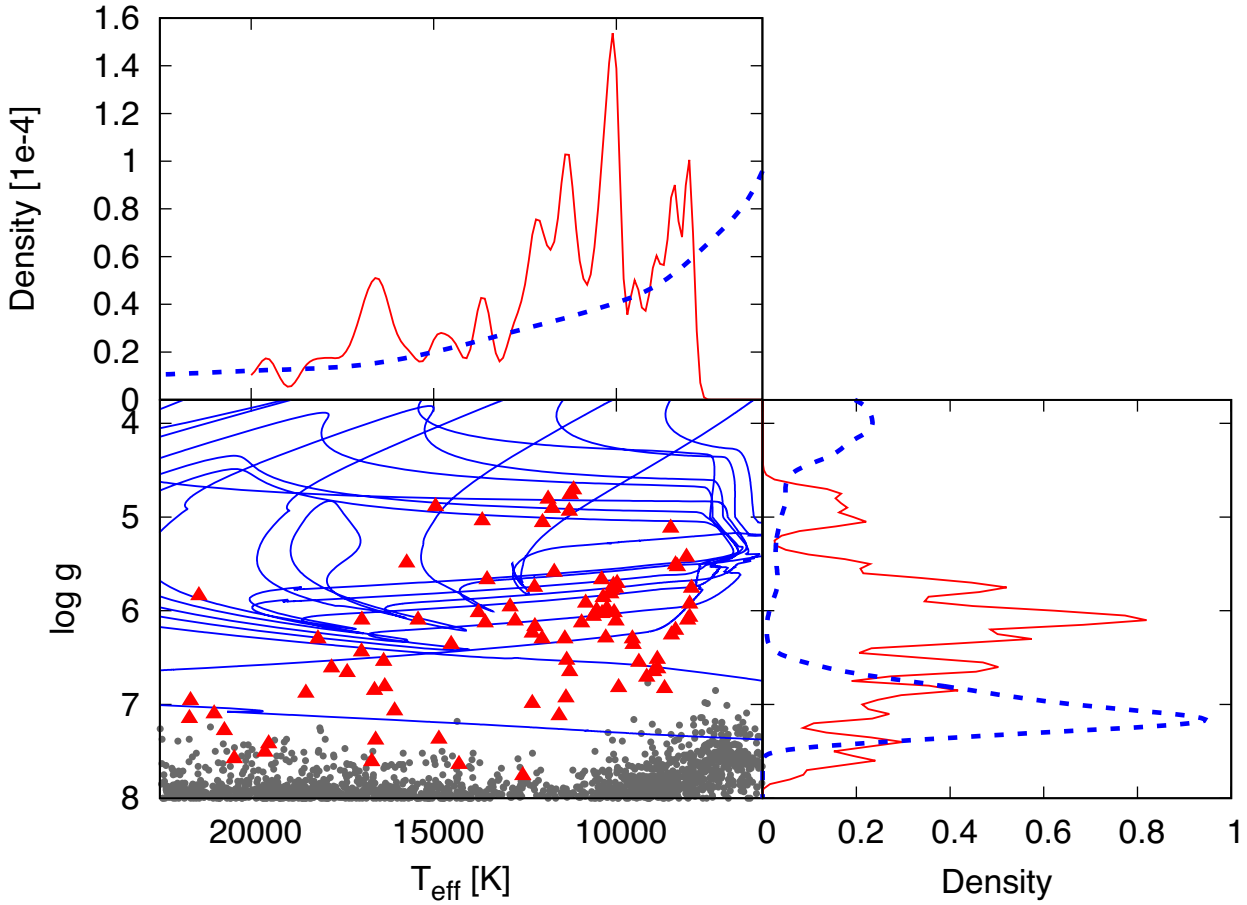

Figure 1. The bottom left panel shows the $T_{\rm eff}$ − log g diagram for objects in the ELM Survey, shown as red triangles, compared with two binary evolution models of Istrate et al. (2016) (blue lines), resulting in ELMs of masses 0.182 and 0.324 $M_{\odot}$. The white dwarfs from Kepler et al. (2016) are shown as grey dots for comparison. The top panel shows the distributions in $T_{\rm eff}$, both for the observed ELMs (red continuous line) and obtained from the models (blue dashed line). The bottom right panel shows the distributions for log$g$. The distributions for the models were obtained taking into account the time spent at each bin of $T_{\rm eff}$ or log g compared with the total evolutionary time, with a spherical volume correction to account for the difference in brightness (see Pelisoli, Kepler & Koester 2018 for further details). Note that there is a lack of known ELMs at the low $T_{\rm eff}$ and low log g ends of the distribution. There are also missing objects around log $g \sim 7.0$; however, this range can also be reached through single evolution.

observed every night for flux calibration, except for Gemini observations, which observed one spectrophotometric standard star per semester.

Time series photometry was obtained with the 1.6-m Perkin–Elmer telescope at Observatório do Pico dos Dias (OPD, Brazil), with an Andor iXon CCD and a red-blocking filter (BG40). We have also used the imaging mode in Goodman at SOAR for photometry, with the S8612 red-blocking filter. The integration time varied from 10–30 s, depending on the brightness of the target, with a typical readout of 1–3 s.

2.2 Data analysis

SOAR spectroscopic data were reduced using IRAF's NOAO package. The frames were first bias-subtracted and flattened with a quartz lamp flat. We then extracted the spectra and performed wavelength calibration with a CuHeAr lamp spectrum extracted with the same aperture. Finally, flux and extinction calibration were applied. The GEMINI IRAF package was used for data from these telescopes and the X-shooter pipeline for the Very Large Telescope (VLT) data, with equivalent steps in the reduction.

Radial velocity estimates were performed with the XCSAO task from the RVSAO package (Kurtz & Mink 1998), after verifying that the intercalated HeAr lamps presented no shift, which was always the case. We cross-correlated the spectral region covering all visible Balmer lines (typically from 3750–4900 Å) with spectral templates from the updated model grid based on Koester (2010), described in Pelisoli et al. (2018). The values of RV were corrected to the Solar system barycentre given the time of observations and the telescope location. All our RV estimates are given in Table A1. We have not added the RVs estimated from the SDSS spectra to our data set, because the SDSS spectra were obtained at least eight years before our data, hence the phase might not be accurate with respect to our recently obtained data.

We performed a Shapiro–Wilk normality test (Shapiro & Wilk 1965) to verify whether the obtained velocities displayed a behaviour that could be explained by Gaussian uncertainties. Next, we calculated the Lomb–Scargle periodogram (Lomb 1976; Scargle 1982) using the NASA Exoplanet Archive tool.[1] For each of

[1] https://exoplanetarchive.ipac.caltech.edu/cgi-bin/Pgram/nph-pgram

Table 1. Followed-up objects and some notable kinematic properties, as well as the SDSS g magnitude. The first 24 objects were followed up spectroscopically only, the next 19 photometrically only and the last two both photometrically and spectroscopically. The quoted proper motions are from Tian et al. (2017), except for J110338.46–160617.4, which is not in this catalogue and for which the proper motion was obtained from Altmann et al. (2017). Many objects show unreliable proper motion, given the relatively faint ($g \gtrsim 18$) magnitude. Note that most objects would be tens of kpc away, given a MS radius.

SDSS J	g	ppm (mas yr^{-1})	$\sigma_{\rm ppm}$ (mas yr^{-1})	$d_{\rm MS}$ (pc)	$d_{\rm (pre-)ELM}$ (pc)	$v_{\rm los}$ (km s^{-1})
004227.73−010634.9	18.63	1.1	2.5	16494	254	111
011508.65+005346.1	18.07	7.5	1.6	16799	232	−173
024932.84−010708.4	19.44	3.2	2.5	27852	405	−146
030608.92−001338.9	16.95	19.3	2.0	6625	108	189
032914.77+003321.8	16.76	11.5	2.3	21652	202	88
045515.00−043231.0	16.49	8.8	2.3	8090	113	64
073934.37+172225.5	18.07	1.4	2.2	10429	173	−65
084034.83+045357.6	17.34	2.7	1.6	9004	140	9
090410.00+034332.9	17.58	3.3	3.1	9697	153	−128
092056.09+013114.8	16.53	12.0	2.1	5346	87	−125
101701.89+070806.8	18.25	6.2	2.9	17876	250	253
112616.66−010140.7	18.50	5.5	2.0	17390	256	62
112620.47+090145.5	18.85	6.2	2.5	23810	331	253
122911.49−003814.4	18.27	10.2	1.8	14079	218	380
142421.30−021425.4	16.93	22.5	1.8	12867	159	14
155937.48+113721.9	17.22	7.4	1.8	30696	270	31
162624.91+162201.5	17.04	6.8	1.8	27991	247	−27
205120.67+014554.4	17.27	9.0	2.4	8954	138	110
213428.63−011409.3	16.96	3.9	2.3	26771	237	142
223831.91+125318.3	15.55	13.6	1.6	3946	61	−18
233343.95−001502.0	19.32	2.2	2.8	26381	382	−16
233403.21+153829.2	16.34	39.1	1.5	3435	62	12
233606.13−102551.5	19.34	5.1	2.7	25693	378	95
233708.62−094307.0	17.90	4.1	1.7	12642	191	−157
045001.34−042712.9	19.07	8.0	3.4	19701	308	−38
073958.57+175834.4	14.75	8.7	2.5	69162	236	−49
075133.48+101809.4	17.40	2.1	2.1	37588	314	−46
075519.92+091511.0	15.32	3.5	1.7	2729	46	−131
075738.94+144827.5	15.04	1.1	1.4	3415	51	−84
092140.37+004347.9	18.39	1.7	2.1	13550	215	−64
094144.89+001233.8	19.28	8.1	2.6	22149	345	−50
104522.80−023735.6	19.28	7.2	2.8	15689	275	101
110338.46−160617.4	15.77	7.3	3.3	5154	75	184
111041.50+132354.3	18.28	19.0	2.4	9648	170	262
112058.97+042012.3	17.87	1.2	2.1	51622	412	158
140353.33+164208.1	16.20	7.7	1.5	5748	85	16
143333.45+041000.8	18.31	2.2	2.3	21349	281	182
160040.95+102511.7	15.00	7.1	1.2	3092	47	94
163625.08+113312.4	17.24	13.0	1.0	12043	164	−215
165700.89+130759.6	15.62	1.5	1.4	4671	68	63
201757.29−125615.6	17.07	4.8	1.7	8796	131	168
204038.41−010215.7	16.59	9.1	1.7	6381	98	165
233625.92+150259.6	17.18	2.6	1.9	9003	134	−160
134336.44+082639.4	16.34	17.5	2.1	5071	81	352
222009.74−092709.9	15.81	9.6	1.6	4659	71	78

the 50 highest peaks in the periodogram, we calculated an orbital solution of the form

$$RV(t) = RV_0 + K \sin(2\pi t/T + \phi), \quad (1)$$

where RV_0 is the systemic velocity, K is the semi-amplitude of the RV variation, T is the period and Φ the phase. We selected as the best solution the one with the highest reduced R^2, defined as

$$R^2 \equiv 1 - \frac{\sum_i (y_i - f_i)^2}{\sum_i (y_i - \bar{y})^2}, \quad (2)$$

where y_i are the observed values, $\bar{y}$ is their mean and f_i are the adjusted values. This is equivalent to selecting the solution with the smallest reduced χ^2.

Each individual spectrum was later Doppler-corrected considering the estimated velocities and all spectra of each object were combined to obtain an $S/N \gtrsim 30$ spectrum (the average for the whole sample was $S/N = 45$). Considering the lack of strong metal lines, we fitted these spectra to a grid of models assuming metallicity $Z = 0.1\ Z_\odot$, with the same input physics as described in Pelisoli et al. (2018). We caution that the quoted uncertainties are formal

fitting errors and the systematic uncertainties are larger. We previously estimated the systematic uncertainties to be ∼5 per cent in $T_{\rm eff}$ and 0.25 dex in $\log g$ (e.g. Pelisoli et al. 2018); however, as we will show in Section 3.4, it seems that the systematic uncertainty in $\log g$ can actually be higher in the $T_{\rm eff}-\log g$ region of the sdAs and can reach 0.5 dex. The SDSS spectra of all objects were also fitted to the same $Z = 0.1\ Z_{\odot}$ grid to allow a comparison. We have relied on the SDSS colours to choose between hot and cool solutions with similar χ^2, which arise due to similar equivalent width being possible with different combinations of $T_{\rm eff}$ and $\log g$. To estimate the mass of each object, we interpolated the models of Althaus et al. (2013). The models of Istrate et al. (2016) made a large improvement to the input physics, by taking into account rotational mixing, which was shown to be an important factor in the atmosphere abundances for ELMs. However, the lowest ELM mass in the models of Istrate et al. (2016) is $0.16-0.18\ M_{\odot}$, depending on the metallicity, and most of our objects show mass lower than that. Only one object (SDSSJ1626+2622) could have its mass accurately determined with the Istrate et al. (2016) models, and this agreed with the mass estimate using Althaus et al. (2013) within the uncertainties. Hence, to be consistent, we used the models of Althaus et al. (2013) for all mass estimates.

All photometry images were bias-subtracted and flat-field corrected using dome flats. Aperture photometry was performed using the DAOPHOT package in IRAF. A neighbouring non-variable star of similar brightness was used to perform differential photometry. The resulting light curve was analysed with PERIOD04 (Lenz & Breger 2005), in search of pulsations with amplitude at least four times larger than the average amplitude of the Fourier transform. PERIOD04 was also used to fit the light curve and perform pre-whitening when pulsations were found and to estimate uncertainties using the Monte Carlo method with 1000 simulations.

3 RESULTS

We found seven objects with RV variations that indicate they are in close binaries. They show p-values smaller than 0.15 for the Shapiro–Wilk test, implying that the variations cannot be explained by Gaussian noise to a confidence level of 85 per cent. For six objects out of these seven, the p-value is smaller than 0.05, hence the confidence level is 95 per cent. The orbital solution shows R^2 larger than 0.95 for all but one object. $T_{\rm eff}$ and $\log g$ suggest they are new (pre-)ELMs. Their properties are given in Section 3.1.

For six other objects, the p-value is larger than 0.15, but we obtain an orbital solution with a short period ($P \lesssim 10$ h), expected from (pre-)ELMs in the range of physical parameters for the sdAs (Brown et al. 2017), and $R^2 \gtrsim 0.85$. Two other objects show $p < 0.05$, but their atmospheric parameters are compatible with both a pre-ELM and a main-sequence star. More data are required to confirm the nature of these eight objects; given the distance modules or proper motion and the estimated physical parameters, we assume they are probable (pre-)ELMs and discuss their properties in Section 3.2.

Six other objects have 12 measurements or more (the average necessary to confirm binarity, according to Brown et al. 2016a), in at least three different epochs and often multiple telescopes, but the Shapiro–Wilk test suggested no real variation. These objects are possibly single stars or show either very short ($\lesssim 1.0$ h) or long periods ($\gtrsim 200$ d). We also found no RV variation or red companions for the five objects observed with X-shooter in three nights over a week. All these objects are detailed in Section 3.3.

In Section 3.4, we compare the values of $T_{\rm eff}$ and $\log g$ obtained by fitting the SDSS spectra and the SOAR or X-shooter spectra for each object. We were unable to obtain a good fit to the Gemini spectra. The Gemini reduction package interpolates between the CCD gaps before performing the flux calibration and that seems to be affecting the output to a point where our models cannot fit the slope of the continuum.

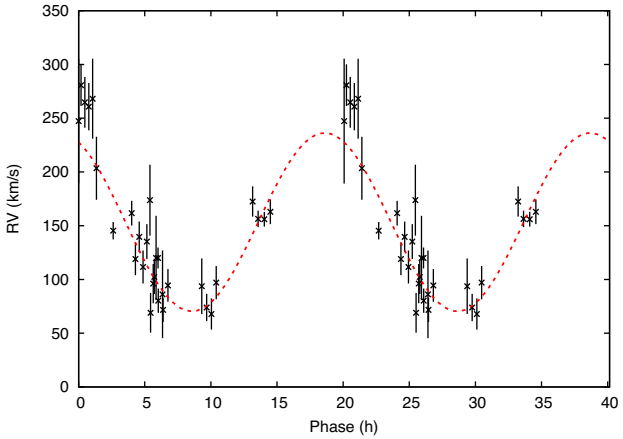

Figure 2. Orbital solution for SDSS J032914.77+003321.8, phase-folded to the 20.1-h period. Note that in this and also the next orbital solution plots, two cycles are shown. The semi-amplitude is $83 \pm 22\ {\rm km\,s^{-1}}$ and the systemic velocity is $153 \pm 18\ {\rm km\,s^{-1}}$.

In addition, we have found seven new pulsators among the sdAs. For 14 other observed stars, we have obtained a detection limit $\lesssim 10$ mmag and found no pulsations. The photometry results are discussed in Section 3.5.

3.1 New (pre-)ELMs

3.1.1 J032914.77+003321.8

The 30 RV estimates for J0329+0033, taken over seven non-consecutive nights at SOAR, yielded a Shapiro–Wilk p-value of 0.004, suggesting with a very high confidence level that the observed variations are not due to chance. We have estimated the period to be 20.1 ± 0.1 h. The semi-amplitude is not well constrained by our data; we estimated it to be $83 \pm 22\ {\rm km\,s^{-1}}$. This results in an orbital fit with $R^2 = 0.78$, shown in Fig. 2, the lowest R^2 among our fits. However, when we assume a main-sequence radius, the photometric parallax gives a distance larger than 20 kpc for this object, which is inconsistent with its proper motion of 11.5 ± 2.3 mas yr^{-1} (Tian et al. 2017). The systemic velocity is also relatively high, $153.3 \pm 18\ {\rm km\,s^{-1}}$. Assuming an ELM radius, the distance drops to ∼200 pc.

Our fit to the SOAR spectrum of J0329+0033 gives $T_{\rm eff} = 9080 \pm 10$ K and $\log g = 5.18 \pm 0.03$. Interpolating the models of Althaus et al. (2013), we obtain $M = 0.1536 \pm 0.0006\ M_{\odot}$. Given this mass and the orbital parameters, the minimal mass of the companion (for an edge-on orbit) is $M_2 = 0.17\ M_{\odot}$, implying a merging time shorter than 765 Gyr.

3.1.2 J073934.37+172225.5

We obtained nine spectra in three nights with SOAR for J0739+1722, the RV variability of which was already suggested by its SDSS subspectra. The RV estimates from the SOAR spectra give $p = 0.1465$. We obtained a period of 6.64 ± 0.03 h, too short for a main-sequence star in the sdA range of parameters (Brown et al.

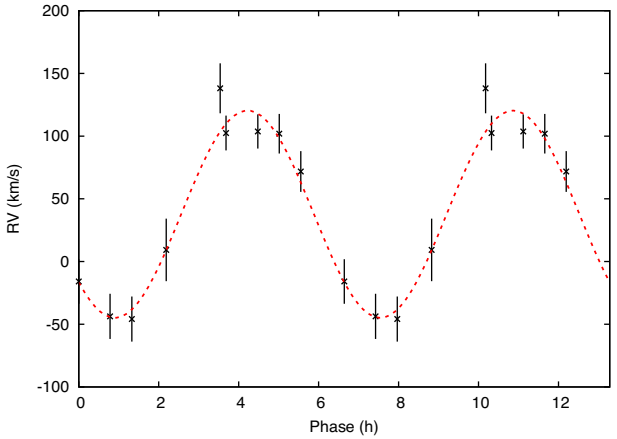

Figure 3. Our orbital fit for J073934.37+172225.5, given the SOAR RV estimates. We obtained $T = 6.61 \pm 0.01$ h, $K = 82.6 \pm 6.8$ km s^{-1}, $RV_0 = 37.8 \pm 3.4$ km s^{-1} and $R^2 = 0.96$.

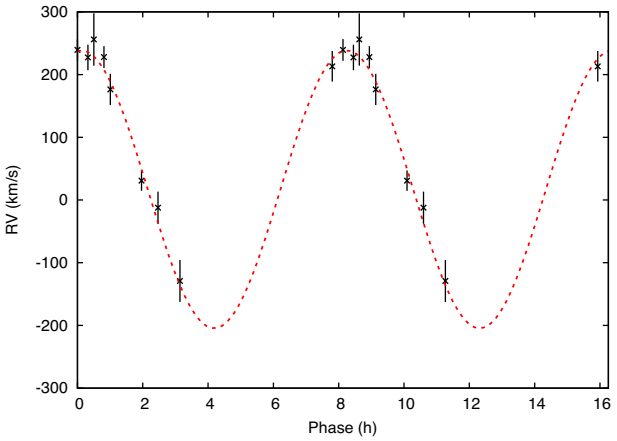

Figure 4. The orbital solution for J084034.83+045357.6, a 0.147-M$_\odot$ pre-ELM with $T_{\rm eff}\sim$ 8000 K. The RV estimates are phase-folded to the 8.13-h period and show a semi-amplitude of $K = 221.6 \pm 12.8$ km s^{-1} and $RV_0 = 17 \pm 13$ km s^{-1}.

2017), and $K = 82.6 \pm 6.8$ km s^{-1}. The orbital solution, shown in Fig. 3, has a high R^2 of 0.96.

We estimated the mass of the ELM primary to be 0.145 ± 0.001 M$_\odot$, given $T_{\rm eff} = 7550 \pm 12$ K and $\log g = 5.06 \pm 0.05$ estimated from the SOAR combined spectrum. The minimum mass of the companion is $M_2 = 0.10$ M$_\odot$. For the mean inclination angle for a random stellar sample, $i = 60$, the mass is 0.12 M$_\odot$. Given the orbital parameters, the merging time is smaller than 68 Gyr.

3.1.3 J084034.83+045357.6

J0840+0453 was observed on three nights with SOAR and we obtained nine spectra. A possible RV variability was first detected in the SDSS subspectra. The Shapiro–Wilk test performed in the SOAR RV data confirmed the variability. The best orbital solution (Fig. 4) gives $R^2 = 0.98$, with a semi-amplitude of 221.6 ± 12.8 km s^{-1} and a period of 8.13 ± 0.01 h.

Our fit to the SOAR spectra of J0840+0453 gives $T_{\rm eff} = 7890 \pm 32$ K and $\log g = 5.07 \pm 0.09$, implying an ELM mass of $M = 0.147 \pm 0.002$ M$_\odot$. The secondary mass is $M_2 > 0.59$ M$_\odot$,

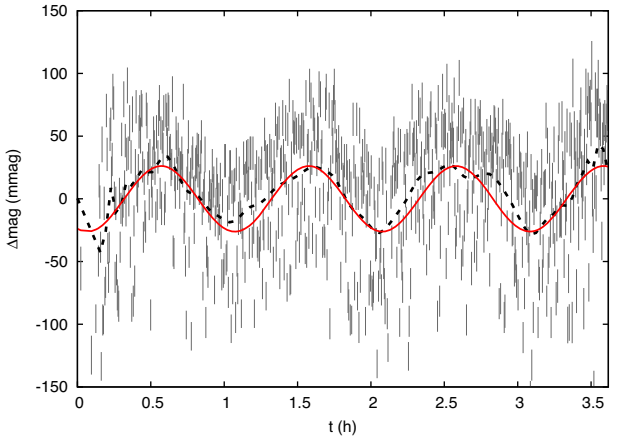

Figure 5. The light curve for SDSS J134336.44+082639.4, obtained at OPD. There is a lot of spread in the data, due to the variation of the seeing throughout the night. The dashed black line shows the smoothed data. The red line shows the best fit obtained with PERIOD04, with a period of 3618 ± 55 s and amplitude of 26.1 ± 2.4 mmag.

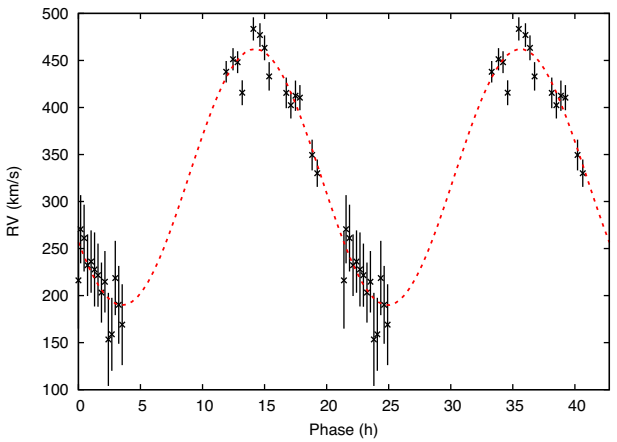

Figure 6. Orbital solution for the photometric variable star SDSS J134336.44+082639.4, with $T = 21.39 \pm 0.01$ h, $K = 136.2 \pm 7.0$ km s^{-1}, $RV_0 = 326.0 \pm 7.2$ km s^{-1} and $R^2 = 0.95$.

hence it is probably a canonical mass white dwarf. The merging time due to gravitational wave radiation is ≤ 28 Gyr.

3.1.4 J134336.44+082639.4

J1343+0826 was found to be photometrically variable in our observations carried out with OPD (see Fig. 5) and most likely ELM by Pelisoli et al. (2018). We found a photometric period of about one hour, with an amplitude of 26.2 ± 2.3 mmag. This is consistent with the predicted values of Córsico & Althaus (2016). Unfortunately, this is the only detected period and therefore we cannot obtain an asteroseismological fit to this object. Spectroscopic follow-up was obtained over five nights at SOAR; 28 spectra were obtained. The derived velocities give $p = 0.004$, indicating variability with a high confidence level (>99 per cent). The dominant period was ∼24 h, a probable alias given that four of the observed nights consisted of two sets of consecutive nights. A similar R^2 (only 0.5 per cent smaller) is obtained with $T = 21.39 \pm 0.01$ h, which is the period we adopt for the orbital solution shown in Fig. 6. The derived semi-amplitude is 136.2 ± 7.0 km s^{-1}. The systemic velocity

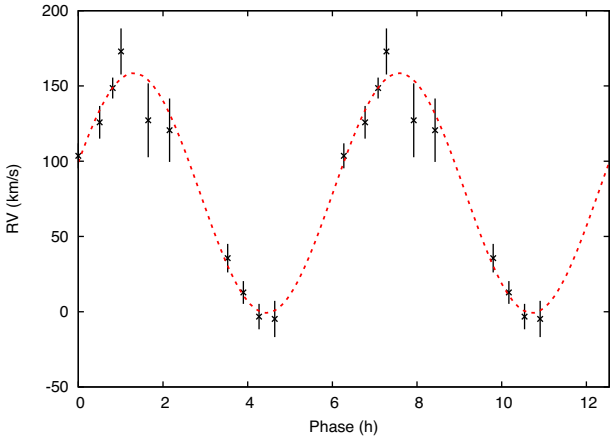

Figure 7. The orbital solution obtained for SDSS J142421.30−021425.4, the RV estimates of which indicated variability at the 85 per cent confidence level.

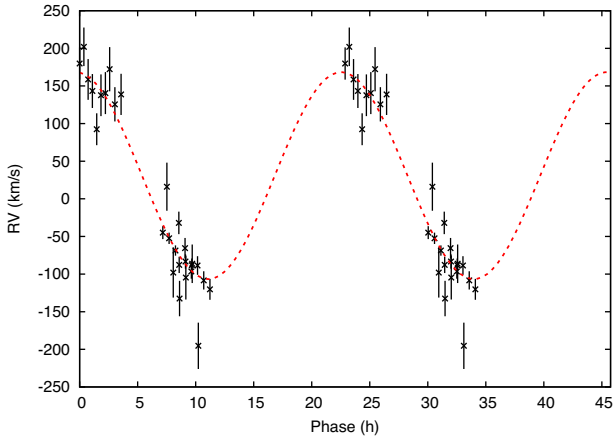

Figure 8. Estimated RVs and orbital solution for SDSS J205120.67+014554.4, which was observed with both SOAR and Gemini. The orbital fit gives $R^2 = 0.93$.

is remarkably high, $RV_0 = 326.0 \pm 7.2$ km s. If the 24.7-h period is the true one, the amplitude would be 175.5 ± 6.8 km s^{-1} and $RV_0 = 323.0 \pm 3.8$ km s^{-1}.

The log g we estimated from the SOAR spectrum of J1343+0826 is among the highest in our sample (5.97 ± 0.03) and the effective temperature is nonetheless quite low ($T_{\rm eff} = 8120 \pm 10$ K), making it a very interesting addition to the known population of pulsating ELMs. We estimate its mass to be $M = 0.153 \pm 0.001$ M$_\odot$, while the companion has $M_2 > 0.43$ M$_\odot$. The objects will merge in less than 449 Gyr.

3.1.5 J142421.30−021425.4

We followed up on J1424−0214, given the RV variability suggested by its SDSS subspectra. We observed it on three nights at SOAR, obtaining 10 spectra. We obtained a period of 6.3 ± 0.4 h, with a semi-amplitude of 79.7 ± 21.8 km s^{-1}. The orbital solution, shown in Fig. 7, has $R^2 = 0.988$.

We derived $T_{\rm eff} = 9300 \pm 11$ K and $\log g = 5.13 \pm 0.03$ from the SOAR combined spectrum assuming one tenth of the solar metallicity, obtaining $M = 0.1558 \pm 0.0008$ M$_\odot$ from the evolutionary models of Althaus et al. (2013). Slightly smaller atmospheric parameters are obtained from the SDSS spectrum, $T_{\rm eff} = 9090 \pm 24$ K and $\log g = 4.53 \pm 0.04$, resulting in $M = 0.170 \pm 0.002$ M$_\odot$. Given the estimated period and semi-amplitude and assuming the parameters derived from the SOAR spectrum are correct, the companion has $M_2 < 0.09$ M$_\odot$ ($M_2 = 0.12$ M$_\odot$ for $q = 60°$) and the objects will merge in less than 57 Gyr.

3.1.6 J205120.67+014554.4

J2051+0145 would be at a distance of ∼9 kpc if it had a main-sequence radius; however, the estimated proper motion of 9.0 ± 2.4 mas yr^{-1} suggests a smaller distance, compatible with a (pre-)ELM radius. Observing it for five nights at SOAR and three nights at Gemini South, we obtained 28 spectra. After obtaining a p-value of only 0.002 (confidence level > 99 per cent), we estimated the period to be 22.9 ± 0.2 h. The semi-amplitude of the orbital solution is 137.5 ± 14.0 km s^{-1} and the systemic velocity is $RV_0 = 30.9 \pm 14.1$ km s^{-1}. The orbital solution is shown in Fig. 8.

The estimates of $T_{\rm eff}$ and log g using the combined SOAR spectrum, 7810 ± 13 K and 5.00 ± 0.05, give $M = 0.148 \pm 0.001$ M$_\odot$.

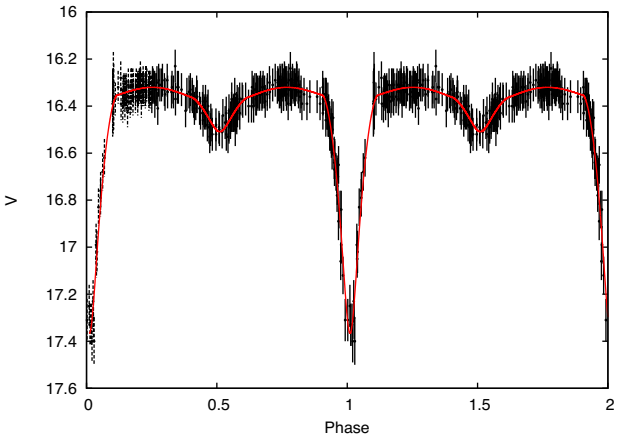

Figure 9. Light curve of J0920+0131, phase-folded to the 15.7-h period. The best fit to the light curve, calculated with JKTEBOP, is shown as a red line.

The minimal mass of the secondary is $M_2 = 0.45$ M$_\odot$ and the merging time due to the emission of gravitational waves is shorter than 533 Gyr.

3.1.7 J092056.09+013114.8 – an eclipsing binary

J0920+0131 is an eclipsing binary identified independently by Palaversa et al. (2013) and Drake et al. (2014). Using data from the the Catalina Real-Time Transient Survey (CRTS: Drake et al. 2009), we estimate the orbital period to be 15.742 ± 0.003 h. The phase-folded light curve is shown in Fig. 9. We obtained 13 spectra in five nights at SOAR. Fixing the period to the photometric estimate, we obtain an orbital solution with $R^2 = 0.95$ (see Fig. 10) and $K = 75.7 \pm 11.5$ km s^{-1}.

We fit the photometry using JKTEBOP (Southworth, Maxted & Smalley 2004) and obtain an orbital inclination of 82.7 ± 0.4 and $R_2/R_1 = 0.80 \pm 0.03$. Given this inclination, we obtain $M_2/M_1 = 0.894$ from the RV fit. Our spectroscopic fit to the spectrum of the primary gives $T_{\rm eff} = 7480 \pm 13$ K and $\log g = 4.80 \pm 0.06$, implying $M_1 = 0.149 \pm 0.002$ M$_\odot$ and $R_1 = 0.25$ R$_\odot$. Therefore the secondary mass seems to be an even lower mass ELM, with $M_2 = 0.133 \pm 0.002$ M$_\odot$ and $R_2 = 0.20$ R$_\odot$. The external uncertainty in the radius, given the 0.25 dex uncertainty in log g, is about

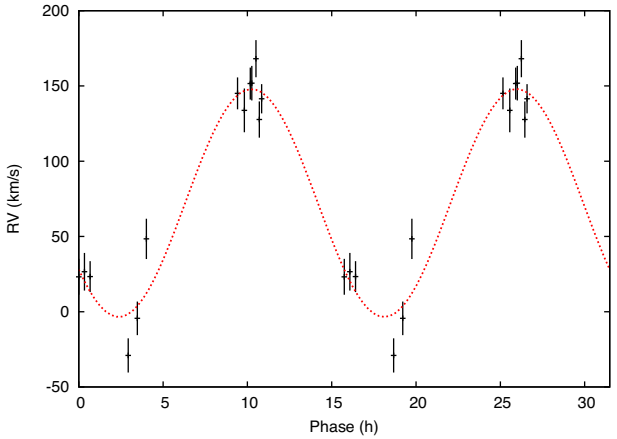

Figure 10. RV data and the obtained orbital solution for SDSS J092056.09+013114.8. The RV data are phase-folded to the photometric 15.7-h period.

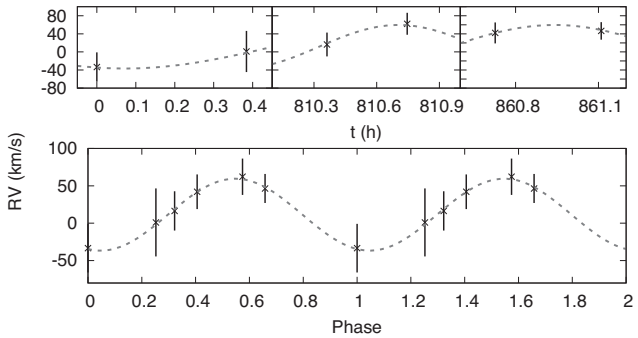

Figure 11. The top panel shows the estimated RVs in the three observed epochs for SDSS J004227.73−010634.9. The bottom panel shows a tentative orbital solution, with a 91-min periodand $R^2 = 0.993$.

0.7 $R_\odot$ (assuming a fixed mass of 0.15 $M_\odot$). Thus the radius of the secondary might be larger, as would be expected from a lower mass white dwarf given the mass–radius relation. We estimate that the secondary shows $T_{\rm eff} \sim 4000$ K, given the ratio between fluxes estimated from the light curve.

3.2 Probable (pre-)ELMs

3.2.1 J004227.73−010634.9

J0042–0106 was followed up because of the $\log g > 5.5$ that we obtained by fitting its SDSS spectrum to solar abundance models. Moreover, assuming the object has a main-sequence radius, we obtain a distance of over 15 kpc. It was observed on three nights with Gemini South; two spectra were obtained on each night. Although the observed variations are consistent with Gaussian errors, we obtained an orbital solution with $R^2 = 0.993$ (Fig. 11). The estimated amplitude is 48 km s^{-1} and the period is quite low, only 91 min. Further observations are required to confirm these findings.

The mass of the primary, given the fit to the SDSS spectrum, which resulted in $T_{\rm eff} = 8050 \pm 24$ and $\log g = 5.51 \pm 0.08$, is $M = 0.1449 \pm 0.0003$ $M_\odot$. Assuming the estimated orbital parameters, we find that the secondary shows $M_2 > 0.028$ $M_\odot$ (for an inclination of 60°, $M_2 = 0.033$ $M_\odot$; for 15°, $M_2 = 0.22$ $M_\odot$). Given the short period, the system would merge in less than a Hubble time ($\tau_{\rm merge} < 4.2$ Gyr).

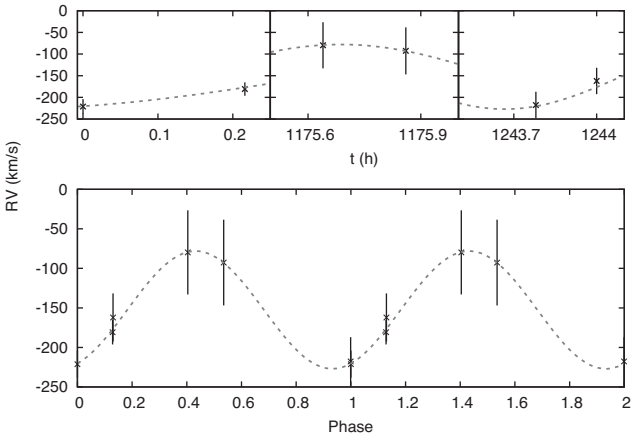

Figure 12. Estimated RVs for SDSS J011508.65+005346.1 (top) and the best orbital solution (bottom). The average uncertainty was 33 km s^{-1}, much larger than our typical values of 10–15 km s^{-1}, due to the bias issue at GMOS South.

3.2.2 J011508.65+005346.1

J0115+0053 also shows $\log g > 5.5$ in our solar abundance fits to its SDSS spectrum and $d > 15$ kpc when a main-sequence radius is assumed. Moreover, we found it to be a more likely ELM in Pelisoli et al. (2018), given its space motion, colours and physical parameters. We obtained six spectra on three nights with Gemini. The RVs obtained show real variability only at a 70 per cent confidence level, but we obtained $R^2 = 0.97$ for the best orbital solution, with $T = 100$ min and $K = 74$ km s^{-1} (see Fig. 12). However, all the spectra were affected by the bright columns that appeared in the Gemini South CCD during the end of 2016B, hence the uncertainties in the velocities are larger.

Given $T_{\rm eff} = 8670 \pm 24$ K and $\log g = 5.64 \pm 0.08$ and the hinted RV variability, we propose that J0115+0053 is a probable ELM, but we caution that more data are needed to confirm this identification. The evolutionary models give a primary mass of 0.150 ± 0.001 $M_\odot$ and, assuming the tentative orbital parameters, the minimal secondary mass is 0.049 $M_\odot$ ($M_2 = 0.058$ $M_\odot$ for $i = 60°$ and $M_2 = 0.54$ $M_\odot$ for $i = 15°$) and the merging time is shorter than 3.2 Gyr.

3.2.3 J030608.92−001338.9

We found J0306–0013 to be most likely a (pre-)ELM in Pelisoli et al. (2018). It was classified as a sdA in Kepler et al. (2016). We obtained 10 spectra over two nights at SOAR. Fitting the combined spectrum to our $Z = 0.1$ $Z_\odot$ grid, we obtain $T_{\rm eff} = 7770 \pm 10$ K and $\log g = 5.36 \pm 0.04$, implying $M = 0.1433 \pm 0.0004$ $M_\odot$. The Shapiro–Wilk test yields $p < 0.3$, suggesting that the estimated RVs vary at the 70 per cent confidence level. With only two nights, it is hard to constrain the orbital period. We find two solutions with R^2 differing by less than two per cent for $T = 28.6$ h and $T = 13.5$ h, the former with $K = 186$ km s^{-1} and the latter with $K = 88$ km s^{-1}. Both solutions are shown in Fig. 13.

For the 28.6-h period, the secondary has a relatively high minimum mass of ∼1.0 $M_\odot$. For any inclination above 60°, the companion would have to be a neutron star. The merging time for this period is smaller than 546 Gyr. On the other hand, for the 13.5-h period, the minimal mass is $M_2 > 0.15$ $M_\odot$ and the merging time is shorter than 320 Gyr.

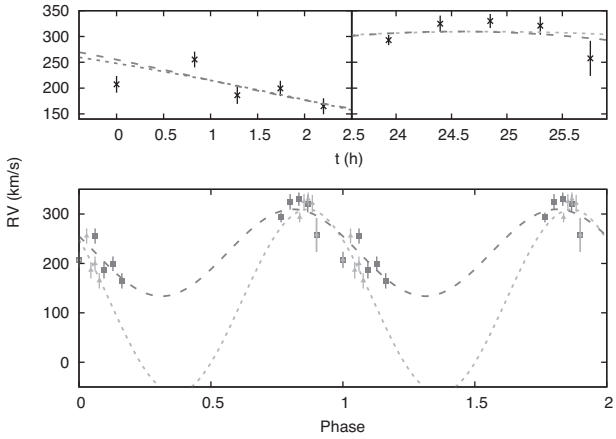

Figure 13. The top panel shows the estimated RVs for SDSS J030608.92−001338.9 on the two observed nights. Two orbital solutions are shown: a short-dashed line (light grey) for the 28.1-h period and a long-dashed line (dark grey) for the 13.1-h period. In the bottom panel, the RVs are phase-folded to these two periods, following the same colour code.

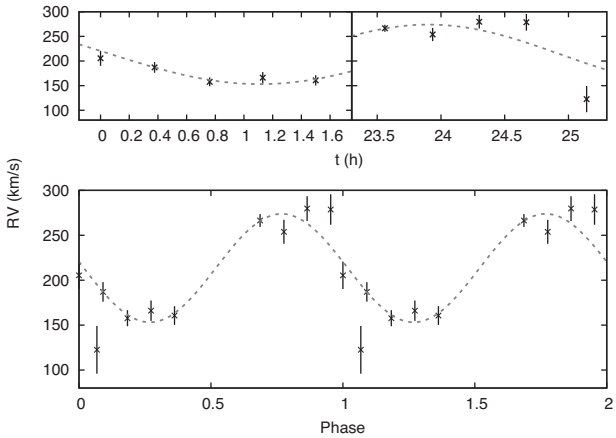

Figure 14. RVs obtained for SDSS J045515.00−043231.0 are shown in the top panel. The bottom panel shows the RVs phase-folded to a 4.1-h period.

3.2.4 J045515.00−043231.0

J0455–0432 was also found to be most likely a (pre-)ELM in Pelisoli et al. (2018). 11 spectra were obtained over two nights at SOAR. The estimated RVs suggest variability at the 65 per cent confidence level. We obtain a dominant period of 4.1 h, but with a high uncertainty of 3.8 h. We estimate $K = 60 \pm 24\,\mathrm{km\,s^{-1}}$. The orbital solution assuming the 4.1-h period, shown in Fig. 14, gives $R^2 = 0.89$.

The SOAR spectrum suggests $T_{\rm eff} = 8250 \pm 8\,\mathrm{K}$ and $\log g = 4.15 \pm 0.03$. These values are consistent with a pre-ELM of $M = 0.180 \pm 0.001\,\mathrm{M_\odot}$, in a binary with an object of minimal mass 0.061 $\mathrm{M_\odot}$ (0.073 $\mathrm{M_\odot}$ for $i = 60^\circ$ and 0.69 $\mathrm{M_\odot}$ for $i = 15^\circ$), which will merge within 25 Gyr.

3.2.5 J122911.49−003814.4

The radial velocity we derived for J1229–0038 from its SDSS spectrum was $472 \pm 3\,\mathrm{km\,s^{-1}}$, consistent with the $465 \pm 5\,\mathrm{km\,s^{-1}}$ given by the SDSS spectral pipeline fit and close to the escape velocity of the Galaxy. Moreover, a main-sequence radius would place it at a distance close to 15 kpc, inconsistent with its proper motion

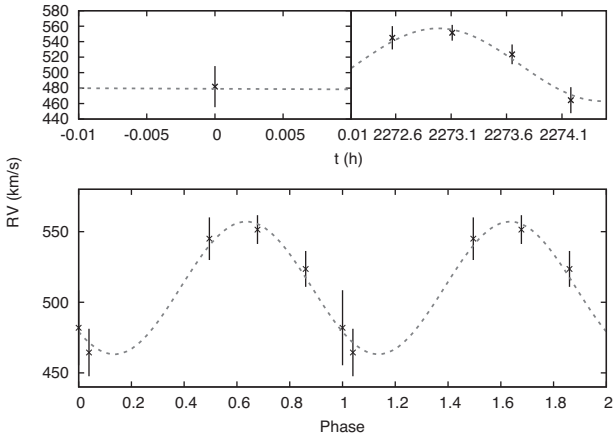

Figure 15. Radial velocities (top) and the best orbital solution (bottom) for SDSS J122911.49−003814.4. The systemic velocity of over 500 $\mathrm{km\,s^{-1}}$ might indicate that the semi-amplitude is much higher than the derived 47 $\mathrm{km\,s^{-1}}$.

of 10.2 ± 1.8 mas $\mathrm{yr^{-1}}$ (Tian et al. 2017). Observing it for two nights at SOAR, we obtained five spectra. Although the Shapiro–Wilk test suggests that the variability can be explained by Gaussian noise, we find an orbital solution with $R^2 = 0.96$, $T = 3$ h and $K = 47\,\mathrm{km\,s^{-1}}$ (shown in Fig. 15). We estimate a very high systemic velocity of $510\,\mathrm{km\,s^{-1}}$, consistent with the SDSS spectrum, suggesting that the semi-amplitude might actually be higher. More data are needed to constrain the orbit of this object.

The fit to its SOAR spectrum gives $T_{\rm eff} = 8300 \pm 21\,\mathrm{K}$ and $\log g = 5.65 \pm 0.06$, implying a mass $M = 0.1476 \pm 0.0009\,\mathrm{M_\odot}$ in the models of Althaus et al. (2013). Assuming the obtained orbital parameters are correct, the mass of the companion should be higher than $M_2 = 0.035\,\mathrm{M_\odot}$, or equal to 0.32 $\mathrm{M_\odot}$ for $i = 15^\circ$. The mass for the most probable $i = 60^\circ$ inclination is 0.042 $\mathrm{M_\odot}$. The merging time is just above a Hubble time, $\tau_{\rm merge} < 20$ Gyr.

3.2.6 J233606.13−102551.5

J2336−1025 would be at a distance larger than 26 kpc if it had a main-sequence radius. We obtained $\log g = 5.72 \pm 0.15$ and $T_{\rm eff} = 8330 \pm 39\,\mathrm{K}$ from its SDSS spectrum using our solar abundance models. This implies $M = 0.149 \pm 0.003\,\mathrm{M_\odot}$ and $R = 0.088 \pm 0.02\,\mathrm{R_\odot}$. We followed it up for three nights with Gemini South, obtaining six spectra. The RV estimates hint at a period of 2.4 h, even though the variability could also be explained by Gaussian uncertainties. The best orbital solution ($R^2 = 0.92$) gives $K = 131\,\mathrm{km\,s^{-1}}$ and is shown in Fig. 16. With these orbital parameters, we obtain $M_2 > 0.12\,\mathrm{M_\odot}$ and $\tau_{\rm merge} < 3.73$ Gyr, shorter than a Hubble time.

3.2.7 J162624.91+162201.5

We obtained in Pelisoli et al. (2018) that J1626+1622 is most likely a (pre-)ELM. It was followed up for two nights at SOAR, when we obtained eight spectra. At a 90 per cent confidence level, the detected RV variability cannot be explained by random uncertainty. We estimated a period of 8.2 ± 0.1 h and $K = 92.6 \pm 19.3\,\mathrm{km\,s^{-1}}$, obtaining an orbital solution with $R^2 = 0.88$, shown in Fig. 17.

However, for J1626+1622 we derived a low $\log g = 3.83 \pm 0.03$, with $T_{\rm eff} = 7460 \pm 15\,\mathrm{K}$, from its combined SOAR spectrum.

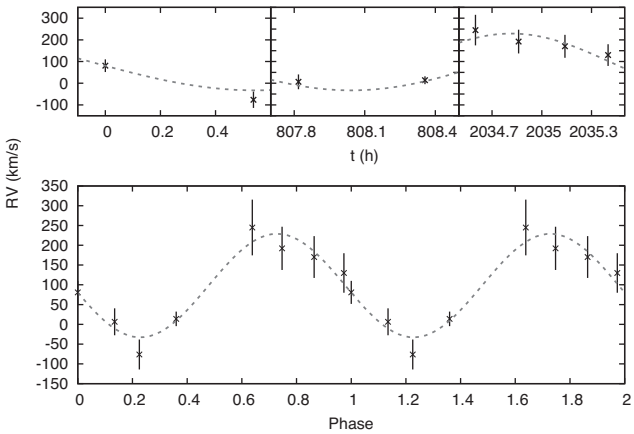

Figure 16. Radial velocity estimates (top) and the best orbital solution (bottom) for SDSS J233606.13−102551.5.

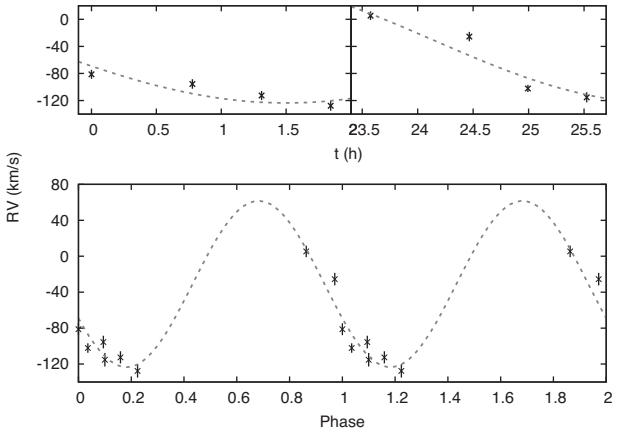

Figure 17. The estimated RVs for SDSS J162624.91+162201.5 are shown in the top panel, while the bottom panel shows the velocities phase-folded to the 8.2-h period, together with the orbital solution.

Similar parameters are obtained from the SDSS spectrum. With these parameters, we could only explain it as a pre-ELM in a CNO flash. The time-scale of these flashes ranges from 10^5–10^6 years. The estimated physical parameters are consistent with the flashes of a $M = 0.34$ M$_\odot$ model. Given the estimated orbital parameters, $M_2 > 0.20$ M$_\odot$ and $\tau_{\rm merge} < 32$ Gyr.

3.2.8 J090410.00+034332.9

We obtained eight spectra over two nights at SOAR for J0904+0343, given its RV variability in the SDSS subspectra. The normality test gave $p = 0.006$, confirming the variability. We estimated a period of 14.7 ± 0.3 h, with a low semi-amplitude of 47.7 ± 2.4 km s^{-1}, suggesting either a high orbital inclination or that the object is a main-sequence binary. The orbital solution, shown in Fig. 18, gives $R^2 = 0.997$.

The J0904+0343 SOAR spectrum fits $T_{\rm eff} = 7680 \pm 20$ and $\log g = 4.08 \pm 0.05$, assuming 0.1 Z$_\odot$. This is compatible with a pre-ELM of mass 0.18 ± 0.05 M$_\odot$ given the models of Althaus et al. (2013). However, it could also mean that the object is a binary metal-poor F star in the halo. The estimated distance given a main-sequence radius is 9 kpc and the proper motion is quite low and uncertain (3.3 ± 3.1 mas yr^{-1}). The low detected semi-amplitude

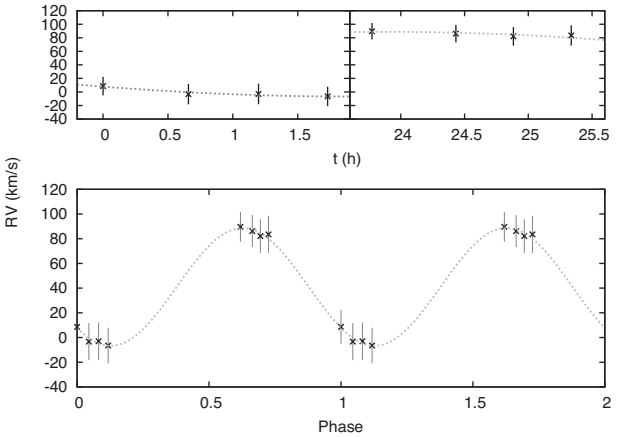

Figure 18. The orbital solution for the SOAR data of SDSS J090410.00+034332.9, folded to a 14.7-h period (bottom), and the estimated RVs (top).

results in a low minimal mass of 0.08 M$_\odot$ assuming a pre-ELM primary, given that the orbit would probably not be edge-on. For a 15° inclination, the mass is about 1.05 M$_\odot$ and for 60° it is 0.092 M$_\odot$. The merging time would be up to 590 Gyr.

We will be able to estimate the distance for this star and others with the parallax to be released by *Gaia* and therefore the difference between our preferred solution as a pre-ELM and a 9-kpc main-sequence star will be clear.

3.3 No detected variation

Fig. 19 shows the RV estimates for those objects with no statistically significant RV variations and no good orbital solutions in the probed ranges of periods, described below. We caution that periods as short as 12 min were observed for the known ELMs (Brown et al. 2011b) and theoretical models predict periods of several days (Sun & Arras 2017).

J222009.74−092709.9 was found to be a photometric variable in OPD data (see Fig. 20). Despite its reliable proper motion of $\mu = 9.6 \pm 1.6$ mas yr^{-1}, we did not find it to be most likely an ELM in Pelisoli et al. (2018), given its colours. The spectroscopic follow-up revealed no orbital periods in the range ∼20 min to ∼200 d. However, we obtain $\log g = 6.10 \pm 0.02$ and $T_{\rm eff} = 8230 \pm 6$ K for the SOAR spectra of this object, which places it not only in the region of the known ELMs but also within the instability strip given by Tremblay et al. (2015), thus justifying the observed photometric variability. We suggest that further monitoring of this object should be carried out to probe shorter and longer orbital periods, as well as further time-series photometry to allow an asteroseismological study.

J233403.21+153829.2, J223831.91+125318.3 and J155937.48+113721.9 also have reliable proper motion according to the criteria of Pelisoli et al. (2018) (39.1 ± 1.5, 13.6 ± 1.6 and 7.4 ± 1.8 mas yr^{-1}, respectively, according to Tian et al. 2017), yet they were not found to be most likely ELMs. J1559+1137 has not been cited previously in the literature. Our estimated physical parameters are close to the main-sequence upper limit, $T_{\rm eff} = 11880 \pm 41$ K and $\log g = 4.83 \pm 0.01$. The lack of RV variation and periods in the range ∼1 h to ∼40 d suggests it is either a short-period or ELM or possibly a halo blue straggler star.

J2343+1538, in particular, was suggested to be an extremely metal-poor (EMP) star by Aoki et al. (2013). Their adopted physical

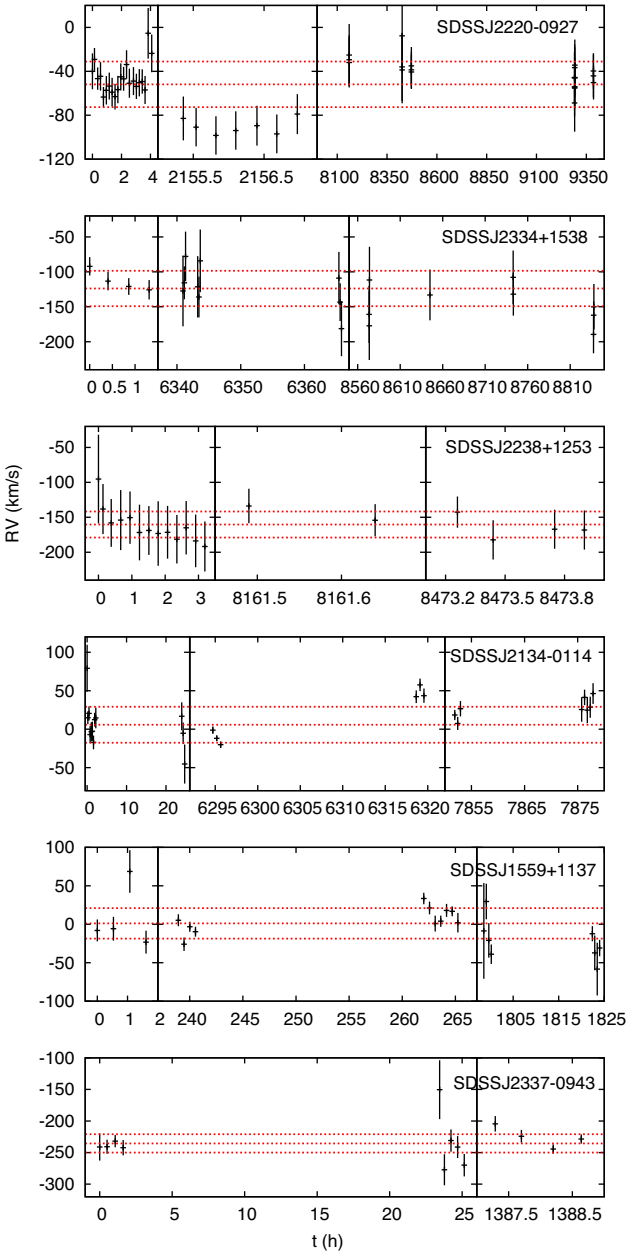

Figure 19. Velocities for the six objects observed in multiple epochs, with no statistically detected variation.

parameters based on the SEGUE stellar parameter pipeline (SSPP: Lee et al. 2008), $T_{\rm eff} = 6500$ K and $\log g = 4.0$, agree within external uncertainties with the parameters we estimate from SOAR spectra, $T_{\rm eff} = 6710 \pm 17$ K and $\log g = 4.25 \pm 0.05$. No periods were found in the ∼24 min to ∼180 d range, thus the EMP explanation seems likely, although at odds with the high proper motion.

J2238+1253 was photometrically classified as a horizontal branch (HB) star by Xue et al. (2008). However, given our estimated physical parameters from its SOAR spectrum, $T_{\rm eff} = 7870 \pm 9$ K and $\log g = 5.17 \pm 0.05$, this classification seems unlikely, considering both the low temperature and high $\log g$. None the less, we find no periods in the range ∼20 min to ∼180 d. The object could be either an EMP with an overestimated $\log g$ or a single ELM, formed through one of the alternative paths to binary evolution described in the Introduction. *Gaia* parallax will allow us to determine its nature.

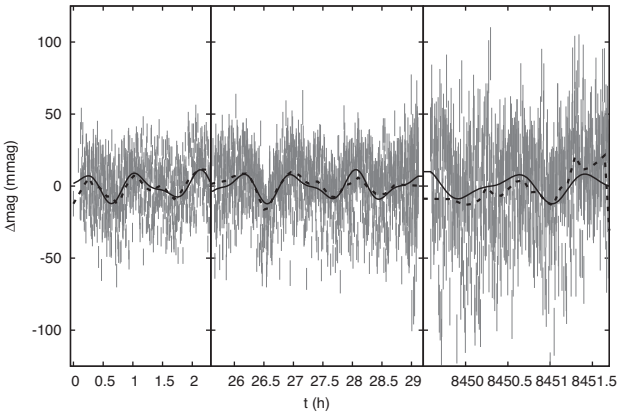

Figure 20. OPD light curve for 222009.74−092709.9. Two periods were found above a detection limit of $4\langle A \rangle$, where $\langle A \rangle$ is the average amplitude of the Fourier transform. The fit to the light curve given these two periods is shown as a continuous line. The dashed line shows the smoothed data.

Table 2. Physical properties derived for the objects observed with X-shooter, with models assuming $Z = 0.1$ Z$_\odot$.

SDSS J	$T_{\rm eff}$ (K)	$\log g$
024932.84−010708.4	8219 ± 13	4.775 ± 0.044
101701.89+070806.8	8746 ± 6	4.331 ± 0.020
112620.47+090145.5	8467 ± 7	4.640 ± 0.021
112616.66−010140.7	8073 ± 8	4.834 ± 0.025
233343.95−001502.0	8279 ± 6	4.410 ± 0.016

J213428.63−011409.3 and J233708.62−094307.0 were both followed up considering the high proper motions (>12 mas yr^{-1}) displayed in the catalogue of Munn et al. (2014). However, both values were actually unreliable due to close-by sources and the proper motions given in the recent GPS1 catalogue (Tian et al. 2017) are much smaller and quite uncertain. For J2134−0114, not only is no RV variation found, but the fit to the SOAR spectrum suggests a relatively low $\log g = 3.76 \pm 0.02$ and $T_{\rm eff} = 12320 \pm 84$ K, placing it above the zero-age horizontal branch (ZAHB). It could thus be a HB star. We cannot, however, discard the possibility that it is a (pre-)ELM in a CNO flash. J2337–0943, on the other hand, lies below the ZAHB, with $T_{\rm eff} = 8020 \pm 12$ K and $\log g = 4.59 \pm 0.06$. Such parameters are consistent with a $M = 0.160 \pm 0.004$ M$_\odot$ pre-ELM, but the non-detection of orbital periods in the range 1 h–30 d and the lack of reliable ($>3\sigma$) proper motion suggest that it could be a metal-poor A/F star instead.

The five objects observed with X-shooter – J024932.84−010708.4, J101701.89+070806.8, J112620.47+090145.5, J112616.66−010140.7 and J233343.95−001502.0 – are shown in Figs 21–25. Their physical properties as estimated from their X-shooter spectra are given in Table 2. Besides the lack of RV variation, it can also be noted that they have no red companions. They all showed $\log g > 5.5$ in our fit to their SDSS spectra assuming solar abundances. Most also show $\log g \gtrsim 5.5$ when $Z = 0.1$ Z$_\odot$ is assumed. Interestingly, the fit to the X-shooter spectra assuming $Z = 0.1$ Z$_\odot$ suggests a $\log g$ lower by ∼1 dex. Possible reasons are discussed in Section 3.4. The parameters obtained and the fact that none shows significant proper motion suggest that they could all be metal-poor A/F stars. However, we caution that they are hotter and apparently less metallic than known low-metallicity stars (e.g Yong et al. 2013).

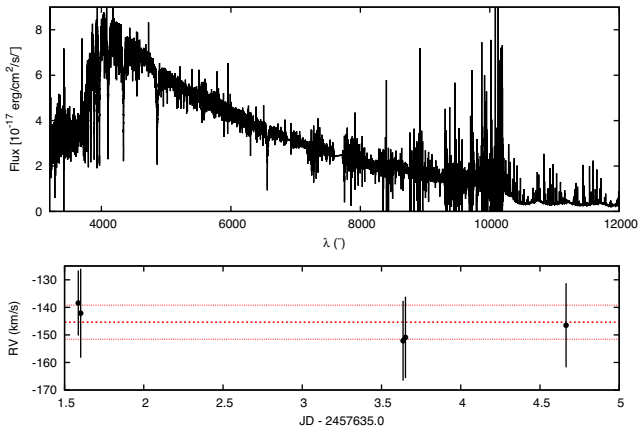

Figure 21. The top panel shows the combined X-shooter spectrum for J024932.84−010708.4. No companion can be identified in the red. The bottom panel shows the RVs obtained for the spectra taken on three different nights. The dashed lines show the weighted mean and the $\pm 1\sigma$ values.

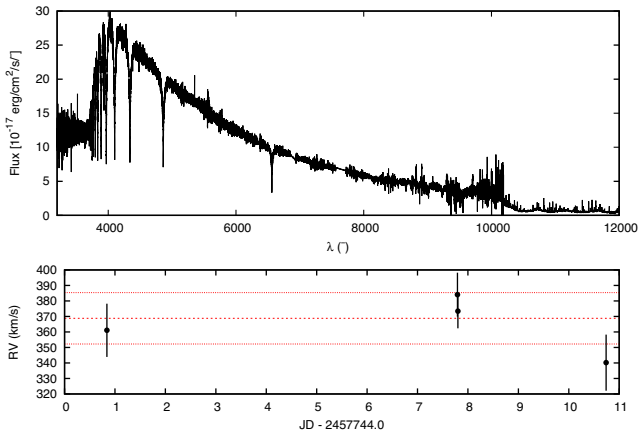

Figure 22. Combined X-shooter spectrum for J101701.89+070806.8 (top) and the RVs obtained from each individual spectrum (bottom). The weighted mean and $\pm 1\sigma$ values are indicated by the dashed lines.

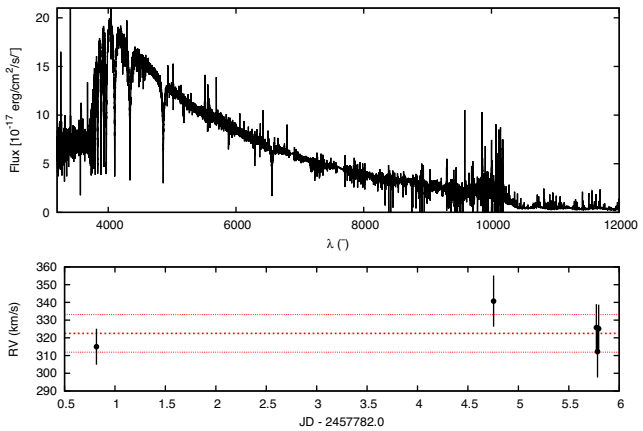

Figure 23. The estimated RVs for J112620.47+090145.5 (bottom), obtained from the individual spectra taken on three different nights. The Doppler-corrected combined spectrum is shown in the top panel.

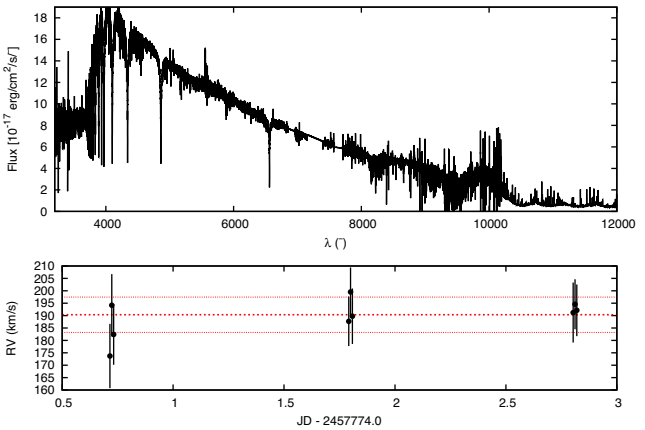

Figure 24. X-shooter spectrum (top) and RV estimates (bottom) for J112616.66−010140.7. The RV estimates agree between the three nights.

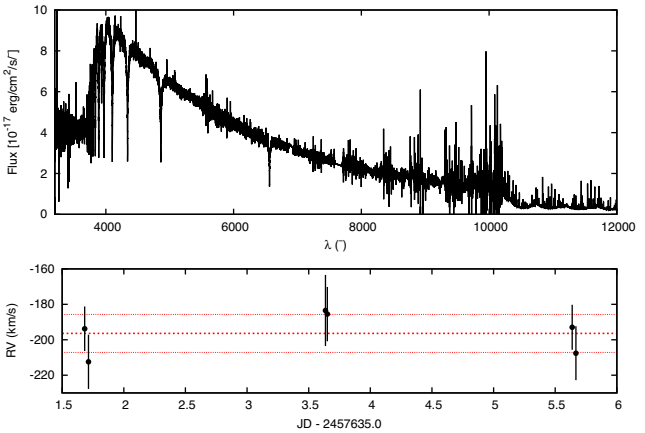

Figure 25. The bottom panel shows the RV estimates for J233343.95−001502.0 and the top panel shows the combined Doppler-corrected spectrum for all epochs.

3.4 Spectral fits

Fig. 26 shows the comparison between our fits to SDSS spectra and spectra obtained as part of this work, with the same grid of models ($Z = 0.1\ Z_{\odot}$). The effective temperature seems to agree remarkably well between spectra obtained with different facilities, with average differences of less than 2 per cent. Log g, on the other hand, shows a larger spread. Considering the spectra obtained with SOAR, the average difference from SDSS, considering only objects with fits not at the border of our grid, is only about 0.08 dex, hence completely consistent with the uncertainties. However, comparing the four X-shooter spectra with SDSS, we obtain a large difference of −0.93 dex. The grid of models is the same, so the difference cannot be explained by metallicity, as suggested by Brown et al. (2017).

The main differences between X-shooter and SDSS/SOAR spectra are the wavelength coverage and the spectral resolution. At low temperatures, the width of the lines is not very sensitive to log g and the log g determination depends essentially on the flux below 3700 Å. Spectra obtained with the SDSS spectrograph only cover above 3800 Å. More recent spectra obtained with BOSS extend the coverage down to 3600 Å, but usually with low *S/N* in this wavelength range. This region is also very sensitive to flux calibration and extinction. Hence log g estimates from SDSS spectra might be

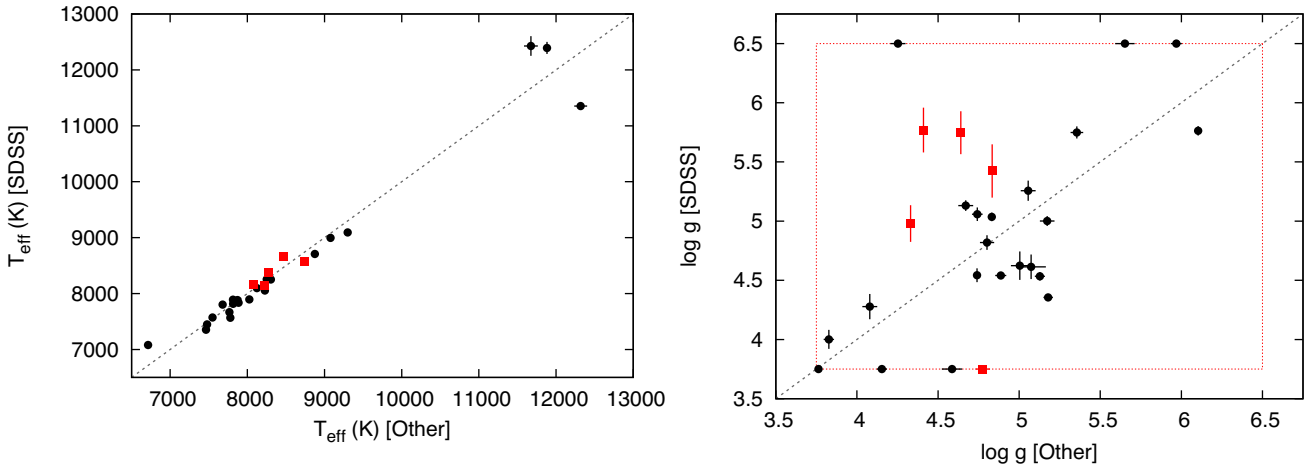

Figure 26. Comparison between the physical parameters obtained by fitting SDSS spectra or SOAR/X-shooter spectra (labelled as other). The physical parameters derived from SOAR spectra are shown as black dots, while parameters derived from X-shooter spectra are shown as red squares. There is a very good agreement, to less than 2 per cent, in $T_{\rm eff}$ (left). The dashed rectangle in the log g panel (right) indicates the border of the model grid. Considering objects within these limits, SOAR and SDSS log$g$ show a low average difference of 0.08 dex. The X-shooter spectra suggest a log g lower by 0.93 dex, which could be due to the better resolution and larger spectral coverage provided by X-shooter, but could also be explained by statistical fluctuations, as detailed in the text.

affected by these uncertainties. We had previously assumed an external 0.25 dex uncertainty (Pelisoli et al. 2018), but it appears that it might be even larger, up to 0.50 dex. It is important to caution, however, that these four objects were selected from a very large sample, with tens of thousands of sdAs (Pelisoli et al. 2018), hence we should expect to find several objects with errors of 2–3σ. In short, we cannot assert that this difference between SDSS and X-shooter spectral fits is systematic, as it might result from statistical fluctuations.

The adopted physical parameters for our new and probable (pre-)ELMs are shown in Table 3, as well as their estimated orbital parameters. Fig. 27 is similar to Fig. 1, including these new objects. These additions to the known sample of ELMs improve the comparison between model predictions and the observed population, by adding objects to both cool and low-mass ends of the (pre-)ELM space of physical parameters.

3.5 Photometry

Besides J1343+0826 and J2220−0927 described in Sections 3.1.4 and 3.3, we have found five other sdAs that show variability. Pulsation periods and amplitudes for all seven objects are shown in Table 4. Two objects, J073958.57+175834.4 and J075519.92+091511.0, show large amplitude variations with periods above 2 h. The estimated parameters from SDSS spectra assuming $Z = 0.1$ Z$_\odot$ are $T_{\rm eff} = 36\,136 \pm 67$ and $\log g = 6.00 \pm 0.02$ for J0739+1758. For J0755+0915, we could not obtain a good fit with the $Z = 0.1$ Z$_\odot$ grid: log g is too close to the lower limit of the grid. For solar metallicity, we obtain $T_{\rm eff} = 7470 \pm 5$ K and $\log g = 4.50 \pm 0.04$. Neither of these two shows significant proper motion. J0755+0915 could be explained as a metal-poor A/F star, but we caution that there is at least one pre-ELM known to show RR Lyrae pulsations (Pietrzyński et al. 2012), given that during the CNO flashes the pre-ELM can reach the RR Lyrae instability strip. J0739+1758 was photometrically selected as a possible AM CVn binary by Carter et al. (2013). However, both the long period and the fact that the SDSS spectrum shows no emission lines seem to rule out this possibility. Its temperature places it within the region where subdwarfs stars show pulsations, hence it could be a new variable subdwarf star. The spectroscopic fit places the object within the domain of V361 Hya stars (first discovered by Kilkenny et al. 1997: $T_{\rm eff} > 28\,000$ K). However, V361 Hya stars usually show p-mode pulsations with short periods (100–400 s). A few were also found to show g-modes (e.g. Schuh et al. 2005), but the g-mode pulsations show low amplitude, unlike what we found. A photometric fit to this object with fixed $\log g = 6.0$ suggests a lower temperature of $T_{\rm eff} = 21\,745 \pm 280$. Our spectral models do not take into account line blanketing by metals or non-local thermodynamic equilibrium (NLTE) effects, which are often important for hot subdwarfs (e.g. Nemeth et al. 2014), hence in this case the spectral parameters should be only taken as a rough estimate. The photometric $T_{\rm eff}$ places the object in the V1093 Her domain (a class first found by Green et al. 2003). V1093 Her stars show g-mode pulsations of the order of hours, as we have observed. The amplitude we observed is nonetheless higher than for the known V1093 Her stars. Further data are required to determine the nature of J0739+1758 better.

A third object, J075738.94+144827.5, was studied in Sánchez-Arias et al. (2018) and found to be more likely a δ Scuti star, given the spacing between periods, a result that should be confirmed by the parallax. Two other new variables, J160040.95+102511.7 and J201757.29−125615.6, are shown in Figs 28 and 29, respectively. The derived physical parameters for the SDSS spectrum of J1600+1025 assuming $Z = 0.1$ Z$_\odot$ are $T_{\rm eff} = 7816 \pm 10$ K and $\log g = 4.63 \pm 0.05$, placing it slightly above the instability strip in Fig. 30. Assuming solar metallicity, the parameters are $T_{\rm eff} = 8050 \pm 8$ K and $\log g = 5.59 \pm 0.03$, placing it within the instability strip of Tremblay et al. (2015). Its proper motion is 7.1 ± 1.2 mas yr^{-1}. For J2017–1256, the derived physical parameters from the SDSS spectra assuming either solar metallicity or $Z = 0.1$ Z$_\odot$ place it slightly above the instability strip. The $Z = 0.1$ Z$_\odot$ parameters are $T_{\rm eff} = 8138 \pm 9$ K and $\log g = 5.14 \pm 0.05$. The proper motion is smaller than 5 mas yr^{-1}, with an uncertainty of almost 2 mas yr^{-1} (Tian et al. 2017). The estimated log g of both objects is too high for δ Scuti stars, which have similar spectral properties to (pre-)ELMs, but show $\log g < 4.4$ (e.g. Murphy et al. 2015). However, given the uncertainties in log g described in Section 3.4, the log g could be lower. We obtain distances of over 3 kpc assuming a main-sequence radius and $z > 1$ kpc given their relatively high

Table 3. Estimated physical and orbital properties for the new and probable (pre-)ELMs, which are separated by a horizontal line. $T_{\rm eff}$ and log g were estimated assuming $Z = 0.1\ Z_{\odot}$. The secondary mass is the lower limit ($i = 90^{\circ}$)and the time for merging is the upper limit. The uncertainties in P and K were calculated with 1000 Monte Carlo simulations in PERIOD04.

SDSS J	$T_{\rm eff}$ (K)	log g	M ($M_{\odot}$)	$P_{\rm orb}$ (h)	K (km s^{-1})	M_2 ($M_{\odot}$)	$\tau_{\rm merge}$ (Gyr)
032914.77+003321.8	9077 ± 10	5.179 ± 0.029	0.1536 ± 0.0006	20.0 ± 0.1	83 ± 22	0.17	765
073934.37+172225.5	7548 ± 12	5.056 ± 0.046	0.1450 ± 0.0011	6.64 ± 0.03	82.6 ± 6.8	0.10	68
084034.83+045357.6	7886 ± 32	5.074 ± 0.091	0.1470 ± 0.0022	8.13 ± 0.01	222 ± 13	0.59	28
134336.44+082639.4	8123 ± 10	5.969 ± 0.034	0.1527 ± 0.0011	24.692 ± 0.002	136.2 ± 7.0	0.43	410
142421.30−021425.4	9299 ± 11	5.128 ± 0.031	0.1558 ± 0.0008	6.3 ± 0.4	80 ± 22	0.09	57
205120.67+014554.4	7813 ± 12	5.004 ± 0.055	0.1476 ± 0.0014	22.9 ± 0.2	138 ± 14	0.45	533
092056.09+013114.8	7478 ± 13	4.802 ± 0.044	0.1492 ± 0.0014	15.742 ± 0.003	75.7 ± 8.1	0.09	50
004227.73−010634.9	8051 ± 24	5.510 ± 0.081	0.1449 ± 0.0003	1.52231 ± 0.00002	48.1 ± 1.6	0.14	4.2
011508.65+005346.1	8673 ± 24	5.641 ± 0.080	0.1499 ± 0.0011	1.678517 ± 0.000009	74.5 ± 5.5	0.05	3.1
030608.92−001338.9[a]	7768 ± 10	5.356 ± 0.039	0.1433 ± 0.0004	28.6 ± 1.1	186 ± 61	1.03	546
				13.5 ± 2.3	88 ± 19	0.15	320
045515.00−043231.0	8251 ± 8	4.154 ± 0.031	0.1796 ± 0.0014	4.1 ± 3.8	60 ± 23	0.06	25
090410.00+034332.9	7680 ± 20	4.079 ± 0.046	0.1810 ± 0.0488	14.7 ± 0.3	47.7 ± 2.4	0.08	590
122911.49−003814.4	8305 ± 21	5.652 ± 0.060	0.1477 ± 0.0009	2.96 ± 0.08	47 ± 5.0	0.04	20
162624.91+162201.5	7464 ± 15	3.827 ± 0.032	0.3454 ± 0.0127	8.2 ± 0.1	93 ± 19	0.20	32
233606.13−102551.5	8328 ± 39	5.716 ± 0.147	0.1487 ± 0.0030	2.38904 ± 0.0008	131 ± 11	0.12	3.7

[a] Two distinct periods are possible with the current data. Parameters for both are shown.

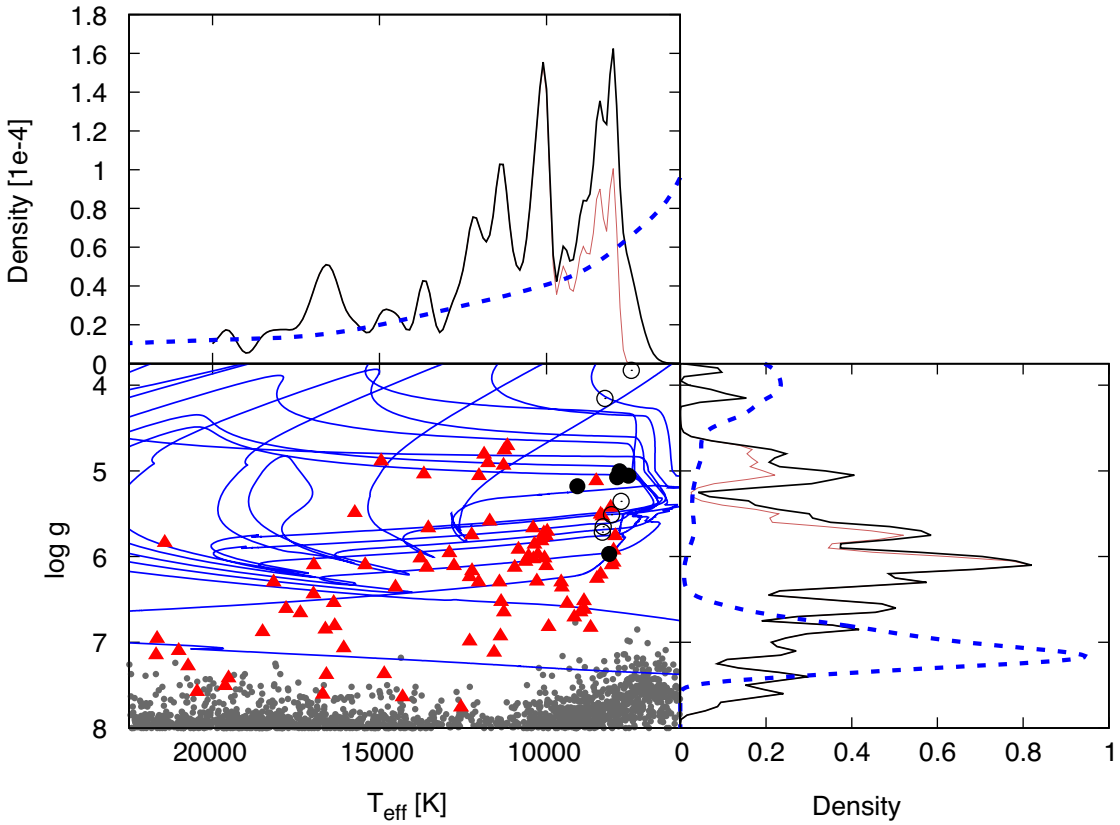

Figure 27. Same as Fig. 1, adding the new (pre-)ELMs (filled black circles) and probable (pre-)ELMs (open black circles). The distributions with these added objects, shown in black, seem more similar to those predicted by the models (dashed blue lines) than the distributions containing only the previously known ELMs (shown in red), especially in $T_{\rm eff}$, the population seems more similar to that predicted by the models. There are still missing (pre-)ELMs at the lower log$g$ end.

Galactic latitude. Unfortunately, the number of periods is insufficient for an asteroseismological analysis, thus conclusions on the nature of these objects require more data.

We have also observed 14 other objects for at least 2 h and for integration times shorter than 30 s and found no pulsations. The observing time and detection limits obtained are shown in Table 5. They are shown in Fig. 30 as not observed to vary, but we caution

Table 4. Periods and amplitudes for all objects found to be photometrically variable, as well as $T_{\rm eff}$ and $\log g$ derived from the SDSS spectra (SOAR for J134336.44+082639.4 and J222009.74−092709.9), assuming $Z = 0.1\ Z_{\odot}$. For J160040.95+102511.7 and J075519.92+091511.0, a good fit is not obtained with $Z = 0.1\ Z_{\odot}$; we then assumed solar metallicity.

Object	$T_{\rm eff}$ (K)	$\log g$	Period (s)	Amplitude (mmag)
J134336.44+082639.4	8120 ± 10	5.97 ± 0.03	26.2 ± 2.4	
J222009.74−092709.9	8230 ± 6	6.10 ± 0.02	3591.24 ± 0.03	7.9 ± 0.7
			2168.8 ± 0.2	3.9 ± 0.7
J075738.94+144827.5	8180 ± 7	4.75 ± 0.04	2437 ± 15	3.3 ± 0.1
			2986 ± 22	2.2 ± 0.1
			2059 ± 16	1.7 ± 0.1
			802 ± 5	0.5 ± 0.1
J160040.95+102511.7	7816 ± 10	4.63 ± 0.05	3849 ± 57	3.1 ± 0.2
			2923 ± 32	1.4 ± 0.2
			2133 ± 21	1.0 ± 0.2
J201757.29−125615.6	8138 ± 9	5.14 ± 0.05	7171 ± 49	9.0 ± 0.5
			3011 ± 58	4.1 ± 0.5
J073958.57+175834.4	36 136 ± 67	6.00 ± 0.02	>11 000	>40
J075519.92+091511.0	7470 ± 5	4.50 ± 0.04	>7800	>100

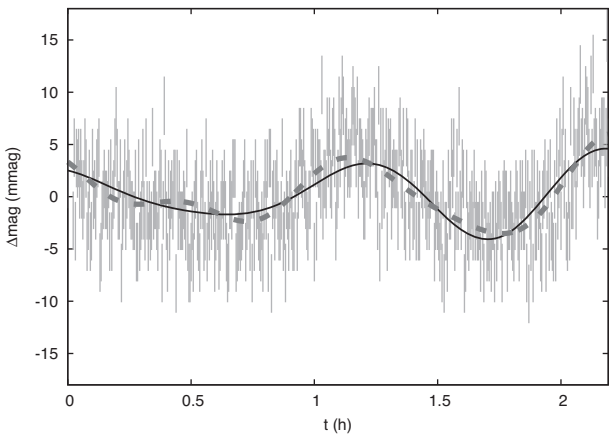

Figure 28. SOAR light curve for 160040.95+102511.7. The grey continuous line is a fit considering the two periods above a 4 ⟨A⟩, 3849 ± 57 s with an amplitude of 3.1 ± 0.2 mmag and 2923 ± 32 s with 1.4 ± 0.2 mmag. The dashed lined adds a third period, which shows an amplitude larger than 3.9 ⟨A⟩, 2133 ± 21 s with 1.0 ± 0.2 mmag.

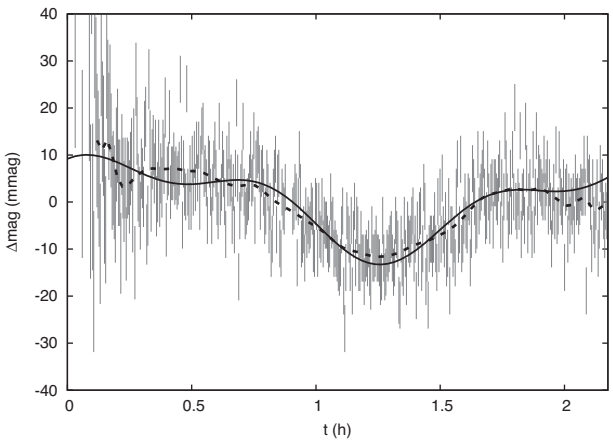

Figure 29. SOAR light curve and best fit (continuous line) for 201757.29−125615.6. We find two periods, 7171 ± 49 s with an amplitude of 9.0 ± 0.5 mmag and 3011 ± 58 s and an amplitude of 4.1 ± 0.5 mmag. Here the dashed line is a smoothing of the data.

that this does not mean they are not variables. Beating can cause destructive interference and essentially hide the pulsations for hours (Castanheira et al. 2007). Moreover, the objects can show pulsations below the detection limit or outside the probed periods.

4 DISCUSSION

With these new pre-ELM and ELM discoveries, we add 12 objects to the $T_{\rm eff} < 9000$ K range. With the three confirmed ELMs in this range given in Brown et al. (2016a), we reach a total of 15 objects, compared with 75 in the $T_{\rm eff} > 9000$ K range (73 confirmed binaries of Brown et al. 2016a, plus J032914.77+003321.8 and J142421.30−021425.4 found in this work). This raises the fraction of cool ELMs from 4 per cent to 20 per cent, which is consistent with the predictions by evolutionary models, considering the uncertainties behind the residual burning.

All of our 15 discoveries show $\log g < 6.0$. Combined with the 26 objects of the ELM Survey in this range, there are now 41 objects at the low-mass end of the ELM distribution. There are 50 objects with $\log g > 6.0$. The fraction is thus close to 1:1; however, the brightness of the lower $\log g$ objects suggests that the fraction could be as high as 100:1 (Pelisoli et al. 2018). Thus, as Fig. 27 already suggested, the population of low-mass objects seems still to be missing. As we considered the estimated $\log g$ as a selection criterion during most of our follow-up, preferring objects with $\log g > 5.0$ or even >5.5, the fact that this population is not unveiled by our work is not surprising, as there are still thousands of sdAs to be observed. With the upcoming data release 2 of *Gaia*, finding this missing population will be a much easier task.

Out of the five observed objects found most likely to be ELMs in Pelisoli et al. (2018) (J0115+0053, J0306–0013, J1626+1622, J1343+0826, J0455–0432), one was confirmed as an ELM and the

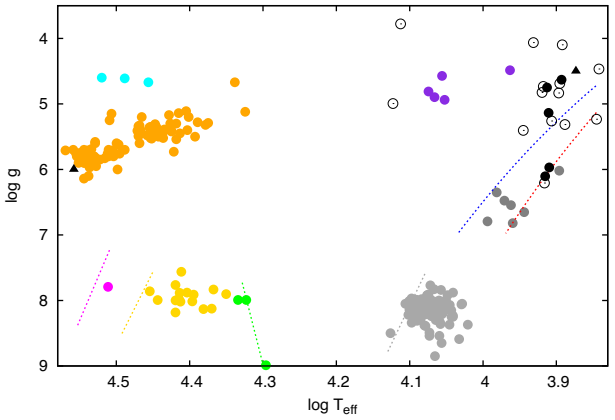

Figure 30. Location of the newly detected variables (filled black symbols) in the $T_{\rm eff}-\log g$ diagram. The triangles are the two objects with high-amplitude pulsations. Open black circles are objects not observed to vary. The hot (blue line) and cool (red line) edges of the ELM instability strip, shown as dotted lines, were extracted from Tremblay et al. (2015). Other pulsating white dwarfs are shown as in fig.1 of Córsico & Althaus (2016): pre-ELMVs (purple), ELMVs (dark grey), DAVs (light grey, bottom right), DQVs (green, at $\log T_{\rm eff}\sim 4.3$), DBVs (yellow) and the only known hot DAV (magenta, bottom left). We have also added the sdV stars from Holdsworth et al. (2017) (orange) and the newly discovered blue large-amplitude pulsators (BLAPs, shown in cyan) from Pietrukowicz et al. (2017) for comparison.

remaining four were found to be probable ELMs. Four of the objects for which we found no RV variability were also studied in Pelisoli et al. (2018), where a higher probability for the MS channel was obtained. It seems that the probability criteria of Pelisoli et al. (2018) are a good indication of the nature of the probed sdAs. On the other hand, ten of the objects we followed up spectroscopically were flagged as possible ELMs in table 1 of Pelisoli et al. (2018) given their $\log g > 5.5$ estimated from SDSS spectra, but only one was confirmed as an ELM (SDSSJ1343+0826) and two others were found to be possible ELMs (SDSSJ0042–0106 and SDSSJ0115+0053). This seems to suggest that the $\log g$ estimate, especially from SDSS spectra, is not a reliable criterion for selecting ELM candidates. This is in line with our findings described in Section 3.4. Spectral coverage of the $\lambda < 3700$ Å region with good *S/N* seems to be a requirement for a reliable estimate of the $\log g$ in this $T_{\rm eff}$ range. This might also explain the discrepancies found by Brown et al. (2017), but a study with a statistically significant sample is required to confirm this.

None of the newly discovered (pre-)ELMs has an orbital period short enough ($\lesssim 1$ h) to be above the predicted detection limit of the upcoming LISA gravitational wave detector. However, such short periods were not probed by our survey, given that most objects were observed with SOAR, a 4.1-m telescope, and required integration times close to 30 min to achieve $S/N \gtrsim 10$ in the individual spectra. Searching for these shorter periods might be interesting for the objects described Section 3.3, especially J2220−0927, which shows not only $\log g > 6.0$ in our spectroscopic fit but also photometric variability with periods in the ELM range.

The objects for which we found no RV variations could alternatively be metal-poor A/F stars in the halo, as already suggested by Brown et al. (2017) as a possible explanation for sdAs. J2343+1538 in particular seems indeed to be an EMP star, as already suggested by Aoki et al. (2013). The five objects observed with X-shooter, which show no significant proper motion, could also be explained as such. J2134−0114 shows parameters consistent with an HB star, but the nature of the other objects remains puzzling. All show $g < 20.0$, therefore they should be included in the DR2 of *Gaia*, making it possible to constrain their radii and determine their nature with certainty. Follow-up will still be required for the objects found to be ELMs in order to estimate their orbital parameters, given that *Gaia* will not be able to resolve binaries with separations below about 20 milliarcsec (∼2 au for a distance of 100 pc).

We have also found seven new photometrically variable stars. J1334+0826 was confirmed as an $M = 0.15$ M$_\odot$ ELM with time-resolved spectroscopy, so it is the eighth member of the ELMV class, adding to the seven known pulsating ELMs (Hermes et al. 2012, 2013a, 2013b; Bell et al. 2015; Kilic et al. 2015). We found no RV variations for J2220−0927, but its estimated $\log g$ and temperature place it inside the instability strip, so it is possibly the ninth member of the class. Time-resolved spectroscopy with larger telescopes, allowing shorter integration times, should be carried out to probe shorter orbital periods for this object. Two other objects, J1600+1025 and J2017–1256, are also found to show pulsations and are within the instability ELMV strip given the uncertainties. Bell et al. (2017) found three pulsating stars among the objects in the ELM Survey showing no radial velocity variations, suggesting that they are related to the sdA population and might be δ Scuti stars with an overestimated $\log g$, which might also be the case for these objects. Hence, as we have not obtained time-resolved spectroscopy for these two stars, we make no claim about their nature given the uncertainties in the $\log g$ estimated from SDSS spectra. Recently, Vos et al. (2018) found evidence of a pre-ELM in a long-period binary (771 ± 3 days), likely the result of a merger of the inner binary in a hierarchical triple system. This is also a possible explanation for the systems for which we find no RV variation at short timescales. Another of the variables we discovered, J0739 +1758, seems to be a sdBV, given its $T_{\rm eff} > 20\,000$ K. Finally, J0755+0915 shows high-amplitude pulsations similar to RR Lyrae stars. The estimated physical parameters and the low proper motion (3.5 ± 1.7 mas yr^{-1} according to Tian et al. 2017) are consistent with a halo metal-poor F star.

5 SUMMARY AND CONCLUSIONS

We present radial velocity estimates and spectral fits for 26 sdAs. We find seven to be new (pre-)ELMs and a further eight others to show most characteristics consistent with (pre-)ELMs, but requiring more data to confirm the detection, hence they are called probable (pre-)ELMs. We perform spectroscopic fits, calculate the best orbital solutions and provide the physical and orbital parameters for each system (Table 3). With these new detections, the percentage of cool ($T_{\rm eff} < 9000$ K) ELMs is raised from 4 to 20 per cent, which is consistent with the predictions of the evolutionary models. Nonetheless there is still a missing population of (pre-)ELMs at the low-mass end, which should be unveiled by *Gaia* DR2. For 11 objects we find no RV variations, ruling out periods larger than ∼1 h and shorter than ∼200 d for most of them. The high rate of identified binaries in the probed sdAs (∼58 per cent) suggests that this evolutionary channel indeed plays an important role in explaining the population, as already suggested in Pelisoli et al. (2018).

We have also found the eighth member of the ELMV class, J1334+0826. A possible ninth member was also identified, J2220−0927, but its binarity was not confirmed by follow-up time-resolved spectroscopy. We found that two other sdAs within the ELM instability strip show pulsations; however, other objects ob-

Table 5. Objects not observed to vary. The physical parameters were estimated from the SDSS spectra assuming $Z = 0.1\ Z_{\odot}$. For J233625.92+150259.6, we have assumed solar metallicity because no good fit could be obtained with $Z = 0.1\ Z_{\odot}$.

SDSS J	$T_{\rm eff}$ (K)	log g	Telescope	Exposure time (h)	3⟨A⟩
092140.37+004347.9	7733 ± 43	5.315 ± 0.179	SOAR	4.0	5.0
143333.45+041000.8	8814 ± 39	5.404 ± 0.157	SOAR	1.8	7.0
233625.92+150259.6	8246 ± 20	6.207 ± 0.061	OPD	2.7	10.0
112058.97+042012.3	13840 ± 265	5.147 ± 0.065	SOAR	2.4	9.0
204038.41−010215.7	7886 ± 19	4.833 ± 0.096	SOAR	1.6	40.0
			OPD	2.2	6.0
163625.08+113312.4	8538 ± 25	4.064 ± 0.060	OPD	4.4	12.0
110338.46−160617.4	8275 ± 10	4.734 ± 0.051	OPD	5.9	10.0
140353.33+164208.1	8062 ± 10	5.261 ± 0.035	OPD	3.0	4.0
165700.89+130759.6	8308 ± 11	4.825 ± 0.047	SOAR	2.6	25.0
			OPD	5.3	10.0
075133.48+101809.4	12954 ± 131	3.779 ± 0.034	SOAR	2.2	1.5
045001.34−042712.9	7797 ± 35	4.098 ± 0.219	SOAR	3.2	8.0
104522.80−023735.6	6950 ± 36	4.467 ± 0.086	SOAR	2.1	7.0
094144.89+001233.8	7859 ± 32	4.689 ± 0.087	SOAR	2.9	6.0
111041.50+132354.3	7859 ± 32	4.689 ± 0.087	SOAR	3.2	6.0

served within the instability strip have shown no variability, suggesting that the strip might not be pure. This should be investigated further when better estimates of the physical parameters of these objects are available, given the possible uncertainty in SDSS spectra that we have identified, due to the lack of good spectroscopic coverage below 3700 Å.

ACKNOWLEDGEMENTS

IP, SOK, ADR and LF acknowledge support from CNPq-Brazil. DK received support from programme Science without Borders, MCIT/MEC-Brazil. IP was also supported by Capes-Brazil under grant 88881.134990/2016-01 and thanks Bruno C. Quint for the assistance in observing runs with SOAR.

Based on observations obtained at Observatório do Pico dos Dias/LNA, at the Southern Astrophysical Research (SOAR) telescope, which is a joint project of the Ministério da Ciência, Tecnologia, Inovação e Comunicações (MCTIC) do Brasil, the US National Optical Astronomy Observatory (NOAO), the University of North Carolina at Chapel Hill (UNC), and Michigan State University (MSU), and at the Gemini Observatory and processed using the Gemini IRAF package, which is operated by the Association of Universities for Research in Astronomy, Inc., under a cooperative agreement with the NSF on behalf of the Gemini partnership: the National Science Foundation (United States), the National Research Council (Canada), CONICYT (Chile), Ministerio de Ciencia, Tecnología e Innovación Productiva (Argentina) and Ministério da Ciência, Tecnologia, Inovaçãos e Comunicaçãoes (Brasil).

REFERENCES

Althaus L. G., Miller Bertolami M. M., Córsico A. H., 2013, A&A, 557, A19
Altmann M., Roeser S., Demleitner M., Bastian U., Schilbach E., 2017, A&A, 600, L4
Aoki W. et al., 2013, AJ, 145, 13
Bell K. J., Kepler S. O., Montgomery M. H., Hermes J. J., Harrold S. T., Winget D. E., 2015, in Dufour P., Bergeron P., Fontaine G., eds, ASP Conf. Ser. Vol. 493, 19th European Workshop on White Dwarfs, Astron. Soc. Pac., San Francisco, p. 217
Bell K. J. et al., 2017, ApJ, 835, 180
Bergeron P., Saffer R. A., Liebert J., 1992, ApJ, 394, 228
Bildsten L., Shen K. J., Weinberg N. N., Nelemans G., 2007, ApJ, 662, L95
Brown J. M., Kilic M., Brown W. R., Kenyon S. J., 2011a, ApJ, 730, 67
Brown W. R., Geller M. J., Kenyon S. J., 2009, ApJ, 690, 1639
Brown W. R., Geller M. J., Kenyon S. J., 2012b, ApJ, 751, 55
Brown W. R., Geller M. J., Kenyon S. J., 2014, ApJ, 787, 89
Brown W. R., Gianninas A., Kilic M., Kenyon S. J., Allende Prieto C., 2016a, ApJ, 818, 155
Brown W. R., Kilic M., Allende Prieto C., Gianninas A., Kenyon S. J., 2013, ApJ, 769, 66
Brown W. R., Kilic M., Allende Prieto C., Kenyon S. J., 2010, ApJ, 723, 1072
Brown W. R., Kilic M., Allende Prieto C., Kenyon S. J., 2012a, ApJ, 744, 142
Brown W. R., Kilic M., Gianninas A., 2017, ApJ, 839, 23
Brown W. R., Kilic M., Hermes J. J., Allende Prieto C., Kenyon S. J., Winget D. E., 2011b, ApJ, 737, L23
Brown W. R., Kilic M., Kenyon S. J., Gianninas A., 2016b, ApJ, 824, 46
Carter P. J. et al., 2013, MNRAS, 429, 2143
Castanheira B. G. et al., 2007, A&A, 462, 989
Clemens J. C., Crain J. A., Anderson R., 2004, in Moorwood A. F. M., Iye M., eds, Proc. SPIE Vol. 5492, Ground-based Instrumentation for Astronomy, SPIE, Bellingham, p. 331
Córsico A. H., Althaus L. G., 2014, A&A, 569, A106
Córsico A. H., Althaus L. G., 2016, A&A, 585, A1
Drake A. J. et al., 2009, ApJ, 696, 870
Drake A. J. et al., 2014, ApJS, 213, 9
D'Cruz N. L., Dorman B., Rood R. T., O'Connell R. W., 1996, ApJ, 466, 359
Foss D., Wade R. A., Green R. F., 1991, ApJ, 374, 281
Gianninas A., Kilic M., Brown W. R., Canton P., Kenyon S. J., 2015, ApJ, 812, 167
Gimeno G. et al., 2016, in Evans C. J., Simard L., Takami H. eds, Ground-based and Airborne Instrumentation for Astronomy VI, SPIE, Bellingham, p. 99082S
Green E. M. et al., 2003, ApJ, 583, L31
Hermes J. J., Montgomery M. H., Winget D. E., Brown W. R., Kilic M., Kenyon S. J., 2012, ApJ, 750, L28
Hermes J. J. et al., 2013a, MNRAS, 436, 3573
Hermes J. J. et al., 2013b, ApJ, 765, 102

Holdsworth D. L., Østensen R. H., Smalley B., Telting J. H., 2017, MNRAS, 466, 5020
Hook I. M., Jørgensen I., Allington-Smith J. R., Davies R. L., Metcalfe N., Murowinski R. G., Crampton D., 2004, PASP, 116, 425
Iben I.,, Jr, Tutukov A. V., 1984, ApJS, 54, 335
Istrate A. G., Marchant P., Tauris T. M., Langer N., Stancliffe R. J., Grassitelli L., 2016, A&A, 595, A35
Kalirai J. S., Hansen B. M. S., Kelson D. D., Reitzel D. B., Rich R. M., Richer H. B., 2008, ApJ, 676, 594
Kepler S. O. et al., 2016, MNRAS, 455, 3413
Kilic M., Brown W. R., Allende Prieto C., Agüeros M. A., Heinke C., Kenyon S. J., 2011, ApJ, 727, 3
Kilic M., Brown W. R., Allende Prieto C., Kenyon S. J., Heinke C. O., Agüeros M. A., Kleinman S. J., 2012, ApJ, 751, 141
Kilic M., Hermes J. J., Gianninas A., Brown W. R., 2015, MNRAS, 446, L26
Kilic M., Munn J. A., Harris H. C., von Hippel T., Liebert J. W., Williams K. A., Jeffery E., DeGennaro S., 2017, ApJ, 837, 162
Kilkenny D., Koen C., O'Donoghue D., Stobie R. S., 1997, MNRAS, 285, 640
Koester D., 2010, Mem. Soc. Astron. Italiana, 81, 921
Kurtz M. J., Mink D. J., 1998, PASP, 110, 934
Lee Y. S. et al., 2008, AJ, 136, 2022
Lenz P., Breger M., 2005, Communications in Asteroseismology, 146, 53
Liebert J., Bergeron P., Holberg J. B., 2005, ApJS, 156, 47
Lomb N. R., 1976, Ap&SS, 39, 447
Marsh T. R., Dhillon V. S., Duck S. R., 1995, MNRAS, 275, 828
Maxted P. F. L. et al., 2011, MNRAS, 418, 1156
Maxted P. F. L. et al., 2014, MNRAS, 437, 1681
Munn J. A. et al., 2014, AJ, 148, 132
Murphy S. J., Bedding T. R., Niemczura E., Kurtz D. W., Smalley B., 2015, MNRAS, 447, 3948
Nelemans G., Tauris T. M., 1998, A&A, 335, L85
Nemeth P., Östensen R., Tremblay P., Hubeny I., 2014, in van Grootel V., Green E., Fontaine G., Charpinet S., eds, ASP Conf. Ser. Vol. 481, 6th Meeting on Hot Subdwarf Stars and Related Objects, Astronomical Society of the Pacific, San Francisco. p. 95
Palaversa L. et al., 2013, AJ, 146, 101
Pelisoli I., Kepler S. O., Koester D., 2017, Open Astronomy, 26, 169
Pelisoli I., Kepler S. O., Koester D., 2018, MNRAS, 475, 2480
Pietrukowicz P. et al., 2017, Nature Astronomy, 1, 0166
Pietrzyński G. et al., 2012, Nature, 484, 75
Robinson E. L., Shafter A. W., 1987, ApJ, 322, 296
Romero A. D., Campos F., Kepler S. O., 2015, MNRAS, 450, 3708
Scargle J. D., 1982, ApJ, 263, 835
Schuh S., Huber J., Green E. M., O'Toole S. J., Dreizler S., Heber U., Fontaine G., 2005, in Koester D., Moehler S., eds, ASP Conf. Ser. Vol. 334, 14th European Workshop on White Dwarfs, Astronomical Society of the Pacific, San Francisco. p. 530
Shapiro S. S., Wilk M. B., 1965, Biometrika, 52, 591
Southworth J., Maxted P. F. L., Smalley B., 2004, MNRAS, 351, 1277
Sun M., Arras P., 2018, ApJ, 858, 14,
Sánchez-Arias J. P. et al., 2018, A&A, arXiv:1804.07318
Tian H.-J. et al., 2017, ApJS, 232, 4
Toonen S., Hollands M., Gänsicke B. T., Boekholt T., 2017, A&A, 602, A16
Tremblay P.-E., Cummings J., Kalirai J. S., Gänsicke B. T., Gentile-Fusillo N., Raddi R., 2016, MNRAS, 461, 2100
Tremblay P.-E., Gianninas A., Kilic M., Ludwig H.-G., Steffen M., Freytag B., Hermes J. J., 2015, ApJ, 809, 148
Vernet J. et al., 2011, A&A, 536, A105
Vos J., Zorotovic M., Vučković M., Schreiber M. R., Østensen R., 2018, MNRAS, 477, L40
Wang B., Han Z., 2009, A&A, 508, L27
Webbink R. F., 1984, ApJ, 277, 355
Woosley S. E., Heger A., 2015, ApJ, 810, 34
Xue X. X. et al., 2008, ApJ, 684, 1143
Yong D. et al., 2013, ApJ, 762, 26
Zacharias N., Finch C., Frouard J., 2017, AJ, 153, 166
Zhang X., Hall P. D., Jeffery C. S., Bi S., 2017, ApJ, 835, 242
Zhang X., Jeffery C. S., 2012, MNRAS, 419, 452

SUPPORTING INFORMATION

Supplementary data are available at *MNRAS* online.

RV_data.dat

Please note: Oxford University Press is not responsible for the content or functionality of any supporting materials supplied by the authors. Any queries (other than missing material) should be directed to the corresponding author for the article.

APPENDIX: RADIAL VELOCITY DATA

Table A1. Radial velocity data for the targets in Sections 3.1, 3.2 and 3.3. The full table is available in the online version of the article.

Object	BJD	RV (km s^{-1})	σ_{RV} (km s^{-1})
J032914.77+003321.8	2457643.8079	247.306	58.121
	2457643.8153	280.711	19.405
	2457643.8273	264.793	23.636
	2457643.8400	260.744	21.986
	2457643.8521	268.121	37.191
	2457643.8639	203.435	29.317
	2457644.8113	161.653	11.512
	2457644.8232	118.973	14.990
	2457644.8351	139.621	14.224
	2457644.8471	111.585	15.353

This paper has been typeset from a TEX/LATEX file prepared by the author.